ELSEVIER

Journal of Magnetism and Magnetic Materials 139 (1995) 263–291

Journal of magnetism and magnetic materials

Theory of magnetostatic waves for in-plane magnetized isotropic films

M.J. Hurben, C.E. Patton *

Department of Physics, Colorado State University, Fort Collins, CO 80523, USA

Received 22 July 1994

Abstract

A modified formulation of the Damon–Eshbach theory of magnetostatic waves for in-plane magnetized isotropic films is presented. Mode dispersion curves and magnetization profiles are examined in detail. Several new results are obtained: (i) Volume mode critical angle effect. (ii) Nonreciprocal volume mode properties. (iii) Volume mode profiles which show quasi-pinning at the film surfaces, even though there are no explicit boundary conditions on the surface spins in the theory. (iv) Physical explanation of the out-of-band surface mode frequencies in terms of the dipole fields for circularly polarized modes. (v) Demonstration of the continuous nature of the change from volume mode to surface mode character for the near-uniform mode at low wave number due to competing dipole field effects.

1. Introduction

Magnetic excitations in solids at microwave frequencies have been a subject of continuing study since the pioneering theory of spin waves by Holstein and Primakoff [1], the discovery of ferromagnetic resonance (FMR) by Griffiths [2], and Kittel's linear response theory for FMR [3]. A special class of magnetic excitations which includes long wavelength propagating modes as well as the usual uniform mode FMR, with the generic name 'magnetostatic modes', have been important for both fundamental reasons and in terms of device applications. These modes typically have characteristic wavelengths which are much shorter than the electromagnetic wavelength. The excitations are termed 'magnetostatic' because for a mode at a given wave number, the mode frequency is *much less* than the corresponding electromagnetic frequency. The label 'magnetostatic modes' is often taken to mean the wavelengths are also sufficiently long that exchange may be neglected. The neglect of exchange, however, has nothing to do with the 'magnetostatic approximation' since the approximation places no lower limit on wavelength. In experiments on real materials, the wavelengths of the excited modes are generally on the order of the size of the sample under study. These excitations have wavelengths which are sufficiently small to satisfy the magnetostatic approximation and sufficiently large, under many circumstances, to neglect exchange.

Numerous papers on the fundamental theory of magnetostatic modes have made significant contributions to the understanding of magnetic excitations in solids. The theory was first done for spheres by

* Corresponding author.

0304-8853/95/$09.50 © 1995 Elsevier Science B.V. All rights reserved
SSDI 0304-8853(94)00561-3

Walker [4]. Here, one obtains various sequences of standing modes which are often termed 'Walker modes'. The mode patterns are much like the normal vibration modes for elastic waves. Röschmann and Dötsch [5] have compiled a practical review of Walker mode theory for spheres.

The theory of magnetostatic mode excitations for ferromagnetic slabs and thin films was first developed by Damon and Eshbach [6]. The theory was for flat, unbounded films or slabs and yielded various propagating modes with wave vectors in the film or slab plane. These propagating modes are often termed magnetostatic waves (MSW). The terms 'magnetostatic modes', 'Walker modes', and 'magnetostatic waves' are often used interchangeably in the literature. The theory of Damon and Eshbach (DE) has served as the basis for numerous experimental studies of magnetic excitations in thin films and slabs of ferrite materials as well as many device applications for microwave signal processing. Two symposia and a recent textbook provide a good review of the device physics and applications for thin slab and film MSW theory [7–9].

The theory of Damon and Eshbach, or the DE theory, yields two types of propagating waves for in-plane magnetized slabs or films: (a) backward volume waves (BVW) for reciprocal in-plane propagation at any angle relative to the field and magnetization direction and (b) a nonreciprocal surface wave for in-plane propagation at angles greater than some critical angle relative to the field and magnetization direction. The term 'reciprocal' denotes modes for which propagation is possible along both $+\boldsymbol{k}$ and $-\boldsymbol{k}$ directions, where $\boldsymbol{k}$ denotes a specific wave vector. 'Nonreciprocal' denotes modes associated with one surface for which propagation is possible only for either $+\boldsymbol{k}$ or $-\boldsymbol{k}$, but not both.

The DE theory was for isotropic ferromagnetic materials. Recent interest in magnetic devices for frequencies in the millimeter wave regime has stimulated a reexamination of high anisotropy ferrites for high frequency use [10,11]. Such materials are desirable for millimeter wave applications because of their large anisotropy fields, up to 20 kOe or more. The proper utilization of such materials can yield FMR peaks at frequencies in excess of 50 GHz for relatively modest magnetic fields. These materials offer unique possibilities for conventional bulk ferrite as well as thin film type millimeter wave devices [12]. In addition to these millimeter wave applications, advances in preparation techniques for magnetic films, magnetic film sandwiches, and magnetic multilayers have resulted in new magnetic properties heretofore unrealized [13]. In many cases, such films have unique anisotropies which can significantly affect the nature of the magnetostatic waves in these structures.

The initial purpose of this work was to examine the effect of magnetic anisotropy on the mode dispersion for magnetostatic waves in thin slabs and films. In the course of the analysis, however, several new and unrealized aspects of MSW excitations for isotropic materials have also been obtained. The aim of this initial report is to review the basic elements of magnetostatic mode theory for isotropic magnetic films and make explicit the nature of these new effects. The most interesting new results for isotropic films concern a critical angle effect and nonreciprocal properties for volume modes and the occurrence of quasi-pinning for volume modes at high wave number.

A second paper will consider modifications in the theory for anisotropic films and examine the effect of these changes on magnetostatic wave properties for several basic categories of anisotropic materials. The most intriguing such property for anisotropic films is in the appearance of *two new* critical angles, one for BVW band inversion to create a forward volume wave (FVW) band of excitations for in-plane magnetized slabs, and one for surface mode/volume wave conversion. This conversion results in a 'reentrant' MSW character in which a uniform mode profile across the film can occur at two distinct frequencies for a given field. The lowest frequency corresponds to FMR. The higher frequency corresponds to a propagating mode with a uniform profile. A third paper will consider out-of-plane magnetized films. Various aspects of these results have been considered previously [14–20]. However, this combined work presents the first comprehensive treatment of magnetostatic modes in isotropic and anisotropic films.

This work does not consider the effects of exchange or the explicit boundary conditions on the dynamic magnetization response at the film surfaces which must be included when exchange is consid-

ered. The inclusion of exchange complicates the theoretical problem greatly. Exchange does lead to important modifications in the theory such as a general lifting of the degeneracy of various MSW dispersion branches in various low- and high-wavenumber limits, as well as branch repulsion. Exchange also brings into play the explicit effect of surface boundary conditions on the dynamic components of the magnetization vector, through pinning effects. Pinning plays no explicit role in the DE theory. However, as will be evident from the analysis below, quasi-pinning effects do occur at large wave numbers. References on exchange effects include Sparks [21], DeWames and Wolfram [22], Wolfram and DeWames [23], Kalinikos [24], and Kalinikos and Slavin [25]. References on pinning include Kittel [26] and Rado and Weertman [27]. Patton [28] has also reviewed the general problem of magnetic excitations and the effects of exchange and surface anisotropy on such excitations.

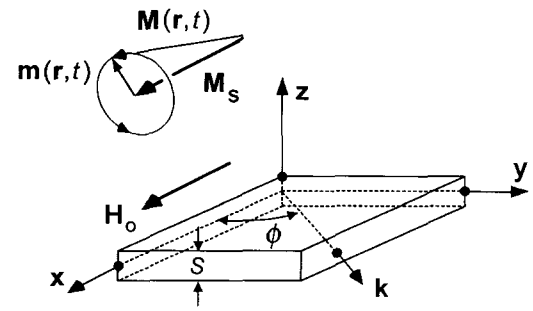

Fig. 1. Film, field, and magnetization geometry for the Damon–Eshbach magnetostatic mode analysis for an in-plane magnetized film of thickness S. The vectors in the $x-y-z$ coordinate system designate the static magnetic field $\boldsymbol{H}_0$, the static saturation magnetization vector $\boldsymbol{M}_s$, and the in-plane wavevector $\boldsymbol{k}$ for a general propagating normal mode. The propagation angle relative to the x-axis is designated by ϕ. The total magnetization response vector $\boldsymbol{M}(\boldsymbol{r},t)$ is shown schematically in the insert, with the precessing $\boldsymbol{M}$-vector separated into two parts, a static component in the x-direction which is equal to M_s and a dynamic magnetization response vector $\boldsymbol{m}(\boldsymbol{r},t)$. The arrow on the precession circle designates the sense of the expected response.

2. Damon–Eshbach formalism for isotropic films

This section and the following three sections summarize and extend the Damon–Eshbach theory for the propagating magnetostatic modes of an isotropic thin film. The key result from the DE theory is in various sets of dispersion curves for volume and surface modes and the corresponding profiles of the dynamic magnetization response across the film for these modes. One obtains two basic kinds of characteristic modes, volume modes for which the profiles correspond to harmonic functions across the film, and a surface mode for which in certain limits the profile is localized at one film surface or the other. For various combinations of wave number, propagation angle, and frequency, one may obtain volume modes, the surface mode, or modes with a mixed character. The volume mode profiles show a little realized effect from the DE theory in the evolution of *quasi*-unpinned modes at low wave numbers to *quasi*-pinned modes at high wave numbers, with asymmetric, *nonreciprocal* behavior for intermediate wave numbers. These features will be made clear in the treatment given below. Finally, in Section 6, the role of dipole fields in determining the lowest order volume mode or surface mode character as a function of propagation angle will be considered explicitly.

Consider a flat unbounded ferromagnetic film which is magnetized by the application of an in-plane external magnetic field. Fig. 1 shows the film, field, and magnetization geometry. The film is taken to be infinite in the x- and y-directions, and with a thickness S in the z-direction. The static magnetic field $\boldsymbol{H}_0$ and the static saturation magnetization vector $\boldsymbol{M}_s$ are both in the x-direction. The objective of the problem is to determine the dynamic propagating normal modes for the film. The wave vector $\boldsymbol{k}$ is shown for a general in-plane propagation direction. The in-plane propagation angle relative to the x-axis is designated by ϕ. The magnetization response vector $\boldsymbol{m}(\boldsymbol{r},t)$ is shown schematically in the Fig. 1 insert. In this classical treatment, one requires that $|\boldsymbol{m}|$ be constant and equal to M_s. The $\boldsymbol{m}$-vector may then be conveniently separated into two parts, a static component in the x-direction which is equal to M_s and a dynamic magnetization response vector $\boldsymbol{m}(\boldsymbol{r},t)$. In the small signal limit in which $|\boldsymbol{m}(\boldsymbol{r},t)| \ll M_s$ is satisfied, to lowest order $\boldsymbol{m}$ has only transverse components m_y and m_z. This transverse response is indicated by the precession circle in the insert. The arrow on the circle designates the precessional nature of the expected response.

In terms of the parameters given above, the specific problem at hand is to obtain and understand the normal mode profiles and corresponding dispersion curves of mode frequency ω vs. wave number k for various ranges of the propagation angle ϕ and static field H_0. The magnetization throughout the material consists of both a large, static, saturation magnetization, and a much smaller dynamic component which results from the precessional motion of the individual dipoles throughout the film. Since the film is of infinite extent in the x- and y-directions, there is no static demagnetizing field to consider. As indicated above, exchange effects are neglected. The normal modes will consist of specific plane waves of the form $m_{y,z} = m_{y0,z0}(z)\exp(\mathrm{i}[\boldsymbol{k}\cdot\boldsymbol{r} - \omega(k)t])$ with specific $m_{y0,z0}(z)$ profile functions which depend on the branch index as well as k, ϕ, H_0, S, and M_s. The $\omega(k)$ dispersion curves for the normal modes will also depend on the branch index, the propagation angle ϕ, the static field H_0, the thickness S, and the saturation magnetization M_s.

The starting point for the DE analysis is the equation of motion for the magnetization $\boldsymbol{M}$,

$$\frac{\mathrm{d}\mathbf{M}}{\mathrm{d}t} = -\gamma(\mathbf{M}\times\mathbf{H})\,. \tag{1}$$

In Eq. (1), γ denotes the gyromagnetic ratio for the electron magnetic moments which make up the material and is taken as positive. For free electron moments corresponding to a Landé g-factor, $g = 2$, one has $\gamma = 1.76\times10^7$ rad/Oe s. To lowest order in transverse components and as indicated above, $\boldsymbol{M}$ is simply given by $\boldsymbol{M} = M_s\boldsymbol{e}_x + m_y\boldsymbol{e}_y + m_z\boldsymbol{e}_z$, where $\boldsymbol{e}_x$, $\boldsymbol{e}_y$, and $\boldsymbol{e}_z$ denote unit vectors in the x-, y-, and z-directions, respectively, and the $m_{y,z}$ have the plane wave form defined above. The total magnetic field $\boldsymbol{H}$ consists of the static x-directed component H_0 already specified and a dynamic field $\boldsymbol{h}(\boldsymbol{r},t)$. To lowest order in transverse components, $\boldsymbol{H}$ has the same form as $\boldsymbol{M}$ and may be written as $\boldsymbol{H} = H_0\boldsymbol{e}_x + h_y\boldsymbol{e}_y + h_z\boldsymbol{e}_z$. The transverse dynamic field components, $h_{y,z}$, have the same form as $m_{y,z}$ and may be written according to $h_{y,z} = h_{y0,z0}(z)\exp(\mathrm{i}[\boldsymbol{k}\cdot\boldsymbol{r} - \omega(k)t])$. It is important to note that the dynamic field $\boldsymbol{h}$ is the total dynamic Maxwellian field obtained self-consistently, along with $\boldsymbol{m}$, from Eq. (1) and Maxwell's equations. In the present context, $\boldsymbol{h}$ may also be viewed as the dipole field generated by the dynamic magnetization $\boldsymbol{m}(\boldsymbol{r},t)$ inside the film.

Eq. (1) leads to a simple magnetic susceptibility connection between $\boldsymbol{m}$ and $\boldsymbol{h}$ [29] which may be written as

$$\begin{pmatrix} 4\pi m_y \\ 4\pi m_z \end{pmatrix} = \begin{pmatrix} \kappa & -\mathrm{i}\nu \\ \mathrm{i}\nu & \kappa \end{pmatrix}\begin{pmatrix} h_y \\ h_z \end{pmatrix}. \tag{2}$$

The κ and ν parameters represent susceptibility functions which are given by

$$\kappa = \frac{\Omega_H}{\Omega_H^2 - \Omega^2} \tag{3}$$

and

$$\nu = \frac{\Omega}{\Omega_H^2 - \Omega^2}\,, \tag{4}$$

where Ω and Ω_H represent reduced frequency and field parameters given by

$$\Omega = \frac{\omega/\gamma}{4\pi M_s} \tag{5}$$

and

$$\Omega_H = \frac{H_0}{4\pi M_s}\,. \tag{6}$$

In the above formulae and for all analyses which follow, the Gaussian system of units is used. Note that Eq. (2) with the κ and ν parameters as defined above is explicitly for an assumed $\exp[-\mathrm{i}\omega t]$ time dependence. Note also that sign inconsistencies are pervasive in the literature. Lax and Button [29], for example, write Eq. (1) without the minus sign, use an $\exp[+\mathrm{i}\omega t]$ time dependence, and obtain the same susceptibility connection given above.

The next step in the Damon–Eshbach analysis is to use the Maxwell equation for $\nabla\times\boldsymbol{h}(\boldsymbol{r},t)$ in the so-called 'magnetostatic' approximation. This approximation is summarized in Appendix A. The approximation is based on the assumption that for a given propagating mode wave number k, the mode frequency ω is much less than the corresponding light frequency at the same wave number, $\omega_l = ck/\sqrt{\varepsilon}$, where c is the speed of light in vacuum and ε is the relative dielectric constant of the material. In this limit, as shown in Appendix A, the $\nabla\times\boldsymbol{h}$ Maxwell equation simply reduces to $\nabla\times\boldsymbol{h} = 0$. Furthermore, this condition is satisfied automatically by expressing $\boldsymbol{h}(\boldsymbol{r},t)$ in terms of a scalar potential $\psi(\boldsymbol{r})$ according to $\boldsymbol{h}(\boldsymbol{r},t) = \nabla\psi(\boldsymbol{r})\exp[-\mathrm{i}\omega t]$. The prob-

lem is now reduced to finding the propagating normal mode solutions for the scalar potential $\psi(\boldsymbol{r})$ which satisfy the $\nabla \cdot \boldsymbol{b} = \nabla \cdot (\boldsymbol{h} + 4\pi \boldsymbol{m}) = 0$ condition, subject to the usual boundary conditions on $\boldsymbol{h}$ and $\boldsymbol{b}$ at the film surfaces. The real power of the Damon–Eshbach formulation is in the use of scalar potentials to obtain relatively simple working equations for mode frequencies and profiles.

The scalar potential function inside the film, corresponding to $|z| < S/2$, is denoted as $\psi^{i}(\boldsymbol{r})$. Outside or external to the film, corresponding to $|z| > S/2$, the scalar potential is specified as $\psi^{e}(\boldsymbol{r})$. These scalar potential functions are then taken as separable and of the form

$$\psi^{i}(x,y,z) = X(x)Y(y)Z^{i}(z) \tag{7}$$

and

$$\psi^{e}(x,y,z) = X(x)Y(y)Z^{e}(z). \tag{8}$$

Note that the $X(x)$ and $Y(y)$ functions are common to both $\psi^{i}(\boldsymbol{r})$ and $\psi^{e}(\boldsymbol{r})$. These functions are constructed to give an in-plane propagating wave at frequency ω and with an in-plane wave vector $\boldsymbol{k}$ as defined in Fig. 1:

$$\boldsymbol{k} = \begin{pmatrix} k_x \\ k_y \\ 0 \end{pmatrix} = k \begin{pmatrix} \cos\phi \\ \sin\phi \\ 0 \end{pmatrix}. \tag{9}$$

The X and Y functions may be written as

$$X(x) = e^{ik_x x} = e^{i(k\cos\phi)x} \tag{10}$$

and

$$Y(y) = e^{ik_y y} = e^{i(k\sin\phi)y}. \tag{11}$$

The relative sizes of k_x and k_y and the corresponding propagation angle ϕ, as well as the sign of k_y, will play an important role in the nature of the Damon–Eshbach normal modes.

The $Z^{i}(z)$ and $Z^{e}(z)$ functions are constructed in accordance with basic symmetry considerations for the film geometry:

$$Z^{i}(z) = a\sin(k_z^{i} z) + b\cos(k_z^{i} z) \quad (|z| < S/2), \tag{12}$$

$$Z^{e}(z) = c\,e^{-k_z^{e} z} \quad (z > +S/2), \tag{13}$$

$$Z^{e}(z) = d\,e^{+k_z^{e} z} \quad (z < -S/2). \tag{14}$$

One has harmonic solutions inside the film and decaying exponential solutions outside the film. Note that the in-plane propagating wave form of the normal modes and the requirement that $\boldsymbol{h}$ and $\boldsymbol{m}$ decay to zero for $|z| \gg S/2$ require that k_x, k_y, and k_z^{e} be purely real and that k_z^{e} also be positive. There are no such restrictions on k_z^{i}. As initially shown by Damon and Eshbach, both real and imaginary values for k_z^{i} are allowed. Real values for k_z^{i} will correspond to harmonic solutions for $Z^{i}(z)$ inside the film. These are the reciprocal volume modes. Imaginary values for k_z^{i} will correspond to a $Z^{i}(z)$ solution which grows or decays exponentially with distance into the film interior from one surface or the other. This is the nonreciprocal surface mode. These points will be considered shortly.

The $\nabla \cdot \boldsymbol{b} = \nabla \cdot (\boldsymbol{h} + 4\pi \boldsymbol{m}) = 0$ condition applied inside the film leads to a relatively simple differential equation for $\psi^{i}(\boldsymbol{r})$:

$$\left[\left(\frac{\partial^2}{\partial x^2}\right) + (1+\kappa)\left(\frac{\partial^2}{\partial y^2} + \frac{\partial^2}{\partial z^2}\right)\right]\psi^{i}(x,y,z) = 0. \tag{15}$$

This equation is simply Laplace's equation with an additional term involving κ. This κ term derives from the magnetization response driven by the κ terms in Eq. (2). Outside the film, one has $\boldsymbol{m} = 0$. The corresponding $\nabla \cdot \boldsymbol{b} = \nabla \cdot \boldsymbol{h} = 0$ condition leads to Laplace's equation for $\psi^{e}(\boldsymbol{r})$:

$$\left(\frac{\partial^2}{\partial x^2} + \frac{\partial^2}{\partial y^2} + \frac{\partial^2}{\partial z^2}\right)\psi^{e}(x,y,z) = 0. \tag{16}$$

The above two equations, along with the functional dependences for $\psi^{i}(\boldsymbol{r})$ and $\psi^{e}(\boldsymbol{r})$ given through Eqs. (7)–(14), immediately yield two connective equations between the various wave number parameters:

$$k_x^2 + (1+\kappa)\left[k_y^2 + (k_z^{i})^2\right] = 0, \tag{17}$$

$$k_x^2 + k_y^2 - (k_z^{e})^2 = 0. \tag{18}$$

Eqs. (17) and (18) define conditions for real or imaginary values of k_z^{i} and different frequency limits for the volume and surface modes. These conditions will be considered in more detail shortly. Eq. (18) also shows that k_z^{e}, the exponential $1/e$ decay rate for $\psi^{e}(\boldsymbol{r})$ outside the film, is simply equal to the propagation wave number $k = (k_x^2 + k_y^2)^{1/2}$.

The remaining steps in the formal Damon–Eshbach analysis are straightforward but tedious. One first applies the usual boundary conditions for the continuity of the parallel components of $\boldsymbol{h}$ and the perpendicular component of $\boldsymbol{b}$ across the film surfaces. The boundary condition on $\boldsymbol{h}$ yields a relatively simple connection between the a and b coefficients in the $\psi^{i}(\boldsymbol{r})$ trial solution of Eq. (12) and the c and d coefficients for the above film and below film $\psi^{e}(\boldsymbol{r})$ trial solutions of Eqs. (13) and (14):

$$a = \frac{c-d}{2}\,\frac{e^{-k_z^e S/2}}{\sin(k_z^i S/2)}, \tag{19}$$

$$b = \frac{c+d}{2}\,\frac{e^{-k_z^e S/2}}{\cos(k_z^i S/2)}. \tag{20}$$

The boundary condition on $\boldsymbol{b}$ then gives a second set of connections between a and b and c and d. The combined set of four equations then yields a further connection between c and d parameters which define the scalar potential amplitudes at the top and bottom film surfaces. This connection between c and d may be written in several forms. One form which will be particularly useful involves the $(c-d)/(c+d)$ ratio, given by

$$\frac{(c-d)}{(c+d)} = \frac{\nu k_y}{(1+\kappa)k_z^i \cot(k_z^i S/2) + k_z^e} = -\frac{(1+\kappa)k_z^i \tan(k_z^i S/2) - k_z^e}{\nu k_y}. \tag{21}$$

The second equality in Eq. (21), in combination with the relation $k_y = k \sin\phi$, yields a general connective equation between the mode frequency and the various wave number parameters,

$$(k_z^e)^2 - (k_z^i)^2(1+\kappa)^2 - \nu^2 k^2 \sin^2\phi + 2k_z^i k_z^e (1+\kappa)\cot(k_z^i S) = 0. \tag{22}$$

From Eqs. (9), (17), and (18), the k_z^i and k_z^e parameters are related to the propagation wave number k by

$$k_z^i = \pm\sqrt{-\frac{1+\kappa\sin^2\phi}{1+\kappa}}\,k \tag{23}$$

and

$$k_z^e = k. \tag{24}$$

Recall that k_z^e and k are defined as real and positive. Note that the mode frequency ω, or equivalently, the normalized frequency Ω, is imbedded in the κ and ν parameters already defined. Considered together, Eqs. (22)–(24) constitute a general dispersion equation for the various normal mode magnetostatic waves of an in-plane magnetized thin film.

Note that neither the z dependence in the scalar potential, defined through the $Z^{i}(z)$ function in Eq. (12) with the coefficients given by Eqs. (19)–(21), nor the dispersion condition of Eq. (22), are affected by a change in sign for k_z^i. In the volume mode analysis to follow, under conditions for which the square root argument in Eq. (23) is positive, k_z^i will be taken as positive. The special case in which the square root argument in Eq. (23) is negative leads to an imaginary k_z^i and the so-called surface mode, to be considered in a later section. Note also, however, that a change in the sign of the propagation angle ϕ can change the normal mode solution through the νk_y term in Eq. (21). This result has important consequences in terms of nonreciprocal mode behavior.

Eqs. (22), (23), and (24) can be reduced to a relatively simple transcendental dispersion equation connecting the mode frequency, the in-plane wave number k, and the propagation angle ϕ. With k_z^i taken as positive, according to the '+' multiplier in front of the square root in Eq. (23), this general dispersion equation is given by

$$(1+\kappa)^2\left(-\frac{1+\kappa\sin^2\phi}{1+\kappa}\right) + \nu^2\sin^2\phi - 1 - 2(1+\kappa)\sqrt{-\frac{1+\kappa\sin^2\phi}{1+\kappa}}\,\cot(k_z^i S) = 0. \tag{25}$$

Note that the square root expression in Eq. (23) appears as a multiplier of the $\cot(k_z^i S)$ in Eq. (25). Note also that k_z^i always occurs in the above equations in combination with the film thickness S, as $k_z^i S$. The wave-number-thickness products $k_z^i S$ and kS will turn out to be useful reduced wave number parameters for the graphical presentation and discussion of dispersion properties.

Recall that the propagating in-plane wave number k is taken as real and positive. This means that the

sign of the expression under the square root sign in both Eqs. (23) and (25) determines whether k_z^i at a given field, frequency, and propagation angle will be real or imaginary. In terms of the reduced frequency and field parameters defined above, this square root expression can be written as

$$-\frac{1+\kappa\sin^2\phi}{1+\kappa}=\frac{\Omega^2-\Omega_H(\Omega_H+\sin^2\phi)}{\Omega_H(\Omega_H+1)-\Omega^2}. \quad (26)$$

The right hand side of Eq. (26) has been written in terms of the reduced frequency parameter $\Omega=\omega/\gamma 4\pi M_s$. This Ω expression is positive only for frequencies within the interval

$$\Omega_H(\Omega_H+1)>\Omega^2>\Omega_H(\Omega_H+\sin^2\phi). \quad (27)$$

Real values for k_z^i are possible, therefore, only within this band of frequencies.

The upper limit in Eq. (27) corresponds to the top of the bulk spin wave band in the limit of low wave number k, with a frequency $\omega_B=\gamma[H_0(H_0+4\pi M_s)]^{1/2}$. This upper volume mode band limit, in reduced DE notation, will be denoted as Ω_B:

$$\Omega_B=\sqrt{\Omega_H(\Omega_H+1)}. \quad (28)$$

The lower limit matches the *bottom* of the bulk spin wave at low k for $\phi=0°$, at a frequency $\omega_H=\gamma H_0$. These spin wave band frequency limits, therefore, also represent the band of volume modes in the Damon–Eshbach theory. Note that as the propagation angle moves from zero to $\pi/2$, the bottom frequency of this volume mode band moves up to meet the top of the band. That is, the volume mode band *collapses to zero width* as the mode propagation angle approaches 90°. This lower volume mode band limit in reduced DE notation will be specified as Ω_A:

$$\Omega_A=\sqrt{\Omega_H(\Omega_H+\sin^2\phi)}. \quad (29)$$

Note that for isotropic materials, Ω_A is *always* below Ω_B. This will not always be the case for anisotropic materials or for an out-of-plane static field. Some important changes in the normal mode properties occur when Ω_A is greater than Ω_B. The present report is concerned only with isotropic materials and in-plane fields. Anisotropic materials and out-of-plane fields will be considered in future papers.

In closing this section, the bulk infinite medium spin wave dispersion equation is included for later reference. The usual form for this equation for saturated materials [30] may be written as

$$\omega_k=\gamma\left[\left(H_0+Dk^2\right)\times\left(H_0+Dk^2+4\pi M_s\sin^2\theta_k\right)\right]^{1/2}, \quad (30)$$

where ω_k is the spin wave frequency, D is an exchange stiffness parameter on the order of 5×10^{-9} Oe cm^2/rad^2 for ferrite materials, and θ_k is the polar spin wave propagation angle relative to the static field $\boldsymbol{H}_0$ and saturation magnetization $\boldsymbol{M}_s$. Note that for wave numbers below about 10^4 rad/cm, the Dk^2 term in Eq. (30) adds a field which is below 0.5 Oe or so and may be neglected. In the present context, with exchange neglected and the $\sin^2\theta_k$ term written in terms of the wave vector components defined above, one may write the spin wave frequency in reduced form as

$$\Omega_k=\left[\Omega_H\left(\Omega_H+\frac{k_y^2+(k_z^i)^2}{k_x^2+k_y^2+(k_z^i)^2}\right)\right]^{1/2}. \quad (31)$$

Note that in the $k_x=0$ limit, Ω_k reduces to Ω_B. In the limit $k_x\to\infty$, Ω_k reduces to Ω_H.

The next section will examine the volume mode dispersion curves and mode profiles from the Damon–Eshbach theory in detail. As already indicated, a normal mode solution is also possible outside the volume mode band of real k_z^i values. This solution will be considered in Section 5.

3. Damon–Eshbach volume modes

As a starting point for the examination of volume mode properties, return briefly to the volume mode frequency band limits discussed above. For fixed values of the material parameters and the applied in-plane field H_0, the upper frequency limit for the band is fixed at a frequency Ω_B as defined above. This upper band limit is independent of the in-plane volume mode propagation angle ϕ. The lower volume mode band limit at Ω_A, however, is not independent of the in-plane volume mode propagation angle ϕ. The Ω_A limit starts out at Ω_H for $\phi=0°$ and propagation parallel to the static field direction.

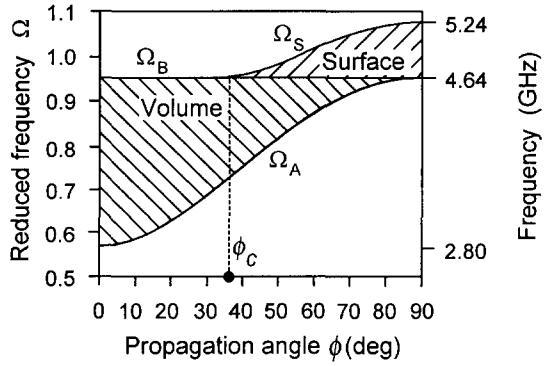

Fig. 2. Volume mode and surface mode bands as a function of in-plane propagation angle ϕ. The Ω_A curve shows the bottom and the Ω_B shows the top of the volume mode band. The curve labeled Ω_S shows the top of the surface mode band, which emerges from the top of the volume mode band at a critical propagation angle ϕ_c. These curves are based on values for the static in-plane field H_0 and the film saturation induction $4\pi M_s$ of 1000 Oe and 1750 G, respectively. The scale on the right side vertical axis gives band limit frequency values in GHz.

As ϕ increases, Ω_A also increases and merges with Ω_B in the $\phi = 90°$ limit for propagation perpendicular to the static field.

Fig. 2 shows a representative plot of the two volume mode band frequency limits, Ω_A and Ω_B, and the corresponding volume mode band as a function of propagation angle ϕ. The curves were calculated for a typical experimental situation for yttrium iron garnet (YIG) films or slabs, with $H_0 = 1000$ Oe and $4\pi M_s = 1750$ G. Ω_B is fixed at 0.947. Ω_A starts out at $\Omega_H = 0.571$ for $\phi = 0°$ and curves upward with increasing ϕ to merge with Ω_B at $\phi = 90°$. The vertical scale on the right side of the figure shows the actual band limit frequencies in GHz. For YIG, one unit in reduced frequency corresponds to 4.9 GHz in practical frequency units. Fig. 2 also shows a third curve labeled Ω_S which emerges from the top of the volume mode band at $\phi = \phi_c \approx 37°$. The band of frequencies between Ω_B and Ω_S corresponds to the surface mode. The propagation angle ϕ_c at which the band begins to form is termed the critical angle for the surface mode. The Damon–Eshbach surface mode will be considered in the next section.

It is important to realize at this point that each propagation angle value in Fig. 2 corresponds to an infinite manifold of dispersion curves of mode frequency vs. wave number, all contained between the frequency limits indicated. By way of example, consider the special case of propagation parallel to $\boldsymbol{H}_0$ and $\boldsymbol{M}_s$, or at $\phi = 0°$. In this special case, Eq. (25) can be written as

$$\cot\left(k_z^i S\right) = F(\Omega) = \frac{1}{2}\left[\sqrt{\frac{\Omega^2 - \Omega_H^2}{\Omega_B^2 - \Omega^2}} - \sqrt{\frac{\Omega_B^2 - \Omega^2}{\Omega^2 - \Omega_H^2}}\right] = \frac{1}{2}\left[\frac{\left(\Omega^2 - \Omega_H^2\right) - \left(\Omega_B^2 - \Omega^2\right)}{\sqrt{\left(\Omega_B^2 - \Omega^2\right)\left(\Omega^2 - \Omega_H^2\right)}}\right]. \tag{32}$$

The right hand side $F(\Omega)$ function of Eq. (32) is written in two slightly different forms. It is clear from the first form that $F(\Omega)$ diverges to $+\infty$ as Ω approaches Ω_B from within the band and to $-\infty$ as Ω approaches Ω_H. The left hand side of Eq. (32), on the other hand, is simply $\cot(k_z^i S)$. This standard function also diverges to $\pm\infty$ at $k_z^i S = 0, \pi, 2\pi, \ldots$

The basic nature of the dispersion solutions can be visualized with the help of Fig. 3, which shows a plot of the first three branch curves of $\cot(k_z^i S)$ vs. $k_z^i S$, shown by the solid lines labeled $n = 1,\ldots,3$, and

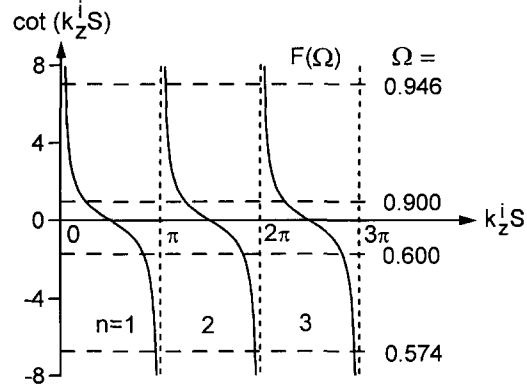

Fig. 3. Plots of the first three branch curves of the function $\cot(k_z^i S)$ vs. $k_z^i S$, shown by the solid lines labeled $n = 1,\ldots,3$, and horizontal cuts across these branch curves which correspond to the $F(\Omega)$ function defined in the text for several values of the reduced frequency Ω between the volume mode band limit frequencies Ω_B and Ω_H. The cuts are based on values for the static in-plane field H_0 and the YIG film saturation induction $4\pi M_s$ of 1000 Oe and 1750 G, respectively, as for Fig. 2.

horizontal cuts across these branch curves which correspond to $F(\Omega)$ for several values of the reduced frequency Ω between Ω_B and Ω_H. All parameters are for a YIG film and a static field of 1000 Oe, as for Fig. 2. The corresponding dispersion solutions for $k_z^i S$ as a function of Ω are indicated by the intersection points between the $\cot(k_z^i S)$ branch curves and the cuts. As Ω moves from Ω_B to Ω_H, the $F(\Omega)$ cut moves from $+\infty$ to $-\infty$, and $k_z^i S$ moves from $(n-1)\pi$ to $n\pi$ for a given branch n. For the first branch, $k_z^i S$ ranges from zero to π as Ω ranges from Ω_B down to Ω_H. For the second branch, $k_z^i S$ ranges from π to 2π as Ω ranges from Ω_B down to Ω_H, and so forth. This means that the standing wave pattern across the thickness of the film for the nth branch evolves from $(n-1)$ half wavelengths to n half wavelengths across the film as one moves from the upper limit frequency Ω_B to the lower limit frequency Ω_H. The first branch, with $n=1$, starts out as a *z-independent* uniform profile with $k_z^i S = 0$ at $\Omega = \Omega_B$. and ends up at $\Omega = \Omega_H$ with $k_z^i S = \pi$. All higher order branches start out at Ω_B with a nonzero value of $k_z^i S = (n-1)\pi$ and end up at $k_z^i S = n\pi$ for $\Omega = \Omega_H$. Mode profiles for these volume modes will be considered at the end of this section. The solution procedure illustrated by Fig. 3 and the discussion above will carry over for nonzero values of the propagation angle ϕ, the surface mode, and anisotropy effects.

The connection with wave number k is obtained from the $\phi = 0$ form of Eq. (23) with positive k_z^i and with κ expressed explicitly in terms of Ω, Ω_B, and Ω_H:

$$k = \sqrt{\frac{\Omega_B^2 - \Omega^2}{\Omega^2 - \Omega_H^2}}\, k_z^i. \tag{33}$$

Eq. (33) shows that for all volume mode branches, the wave number k will *always* begin at zero at the top of the band for $\Omega = \Omega_B$ and *diverge* to infinity as the frequency moves to the bottom of the band at $\Omega = \Omega_H$. While the map itself between Ω and k will depend on the particular $k_z^i S$ branch selected, the end points will not be branch dependent. All branches will begin at $k = 0$ and $\Omega = \Omega_B$, and all branches will end at $k = \infty$ and $\Omega = \Omega_H$.

Fig. 4 shows plots of various volume mode dispersion branches for the same field and YIG saturation induction values used for Figs. 2 and 3, and the $\phi = 0°$ propagation direction case just discussed. The plots are for reduced frequency Ω as a function of the reduced wave number kS product. The solid lines represent dispersion curves based on Eqs. (32) and (33). The n-values indicate the order of the dispersion curves, with $n = 1$ for the initial $k_z^i S$ range from zero to π already discussed, $n = 2$ for $\pi < k_z^i S < 2\pi$, etc. and so forth. As in Fig. 2, the left side vertical axis shows reduced frequency Ω and the right side axis shows band limit frequencies in GHz. The horizontal axis shows values of kS from zero to 35.

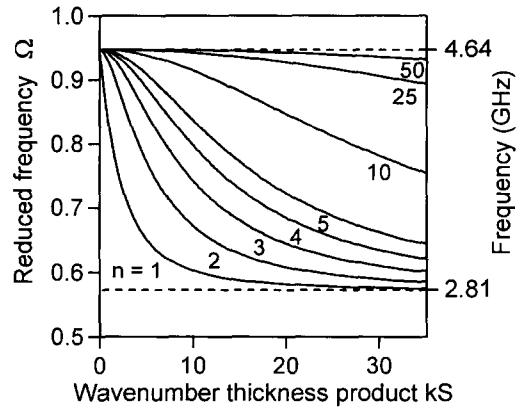

Fig. 4. Volume mode dispersion curves of reduced frequency Ω vs. in-plane wavenumber thickness product kS for propagation parallel to the in-plane static field with an in-plane propagation angle $\phi = 0°$. All curves are based on values for the static in-plane field H_0 and the film saturation induction $4\pi M_s$ of 1000 Oe and 1750 G, respectively, as for Fig. 2. The scale on the right side vertical axis gives frequency band limit values in GHz. The n-values designate the order of the corresponding $\cot(k_z^i S)$ branch solution.

It is clear from Fig. 4 that there is an infinite manifold of volume mode dispersion curves. All curves start at $\Omega = \Omega_B$ in the $kS = 0$ limit. In the limit of very large kS values, all curves approach the lower frequency limit of the volume mode band at $\Omega = \Omega_H$. For the in-between range of kS values, the dispersion curves have negative slopes and cover the entire volume mode band. The negative slopes correspond to negative values for wave packet group velocities defined by $v_g = \partial\omega/\partial k$. These negative group velocities, in turn, have led to the label 'backward volume wave' for these modes.

It was already noted that this volume mode fre-

quency band is the same as the bulk spin wave band in the limit of low wave number. It is clear, therefore, that this volume mode band of dispersion curves represents an extension of the bulk spin wave band to low wave numbers for which the film surfaces become important. It is noteworthy that the lowest order dispersion curve labeled $n = 1$ has a nonzero slope in the low kS limit, while all higher order curves approach $\Omega = \Omega_B$ with zero slope. This nonzero slope is connected with the special nature of the $n = 1$ branch solution of Eq. (32) at $k_z^i S = 0$ for $\Omega = \Omega_B$. As already discussed, $k_z^i S = 0$ corresponds to the uniform mode and a dynamic magnetization $\boldsymbol{m}(\boldsymbol{r},t)$ which is $\boldsymbol{r}$-independent and constant across the film. The combination of this $k_z^i S \to 0$ condition with the $kS \to 0$ in the $\Omega \to \Omega_B$ limit leads to this nonzero slope for the lowest order $n = 1$ dispersion branch.

The shapes of the curves in Fig. 4 can be understood on physical grounds. First, consider the common frequency at $\Omega = \Omega_B$ in the $kS = 0$ limit for all of the modes. The $n = 0$ mode simply corresponds to ferromagnetic resonance (FMR) for an in-plane magnetized thin film, with an FMR frequency of Ω_B. The higher order modes, in this limit, all have effective wave vectors given by $k_z^i \boldsymbol{e}_z$. These wave vectors are all perpendicular to $\boldsymbol{H}_0$ and, hence, correspond to spin wave modes propagating perpendicular to $\boldsymbol{H}_0$ as well. In the limit of small exchange effects, such spin waves also have a common frequency equal to Ω_B. This result is also contained in the spin wave dispersion in Eq. (31) for $k_x = k_y = 0$. The approach of all branch frequencies to Ω_H in the limit of very large values of kS can also be understood from the spin wave model. In this limit, the predominant wave vector for all modes is simply $k\boldsymbol{e}_x$. Such a wave vector is parallel to $\boldsymbol{H}_0$ and corresponds to spin wave frequencies at the bottom of the spin wave band at $\Omega = \Omega_H$. Finally, consider the knee, or point at which the different branches begin to level off as kS increases. The knee of the $n = 1$ dispersion curve occurs at approximately $kS \approx 5$–10. This knee moves to larger and larger kS values for increasing values of the branch index n. With $k_z^i S$ on the order of $n\pi$ for a given branch, the knee occurs when the value of kS begins to exceed $k_z^i S$, and the direction of the effective k-vector $\boldsymbol{k}_{\text{eff}} = k\boldsymbol{e}_x + k_z^i \boldsymbol{e}_z$ becomes more parallel than perpendicular to $\boldsymbol{H}_0$.

The above discussion of the volume mode dispersion curves has been limited so far to the case of propagation parallel to the static field $\boldsymbol{H}_0$ at $\phi = 0°$. Consider now the effect on the family of backward volume wave dispersion curves when the propagation angle ϕ is rotated away from 0°. The behavior of the band limits Ω_A and Ω_B as a function of the propagation angle ϕ have already been discussed in connection with Fig. 2. The operational equations for the actual dispersion branch solutions now come from Eqs. (23) and (25) with ϕ 0°. After some manipulation, these equations may be rewritten for the frequency range $\Omega_A < \Omega < \Omega_B$ according to

$$\cot\left(k_z^i S\right) = G(\Omega) = \frac{1}{2}\left[\frac{\left(\Omega^2 - \Omega_A^2\right) - \left(\Omega_B^2 - \Omega^2\right) - \sin^2\phi}{\sqrt{\left(\Omega_B^2 - \Omega^2\right)\left(\Omega^2 - \Omega_A^2\right)}}\right] \tag{34}$$

and

$$k = \sqrt{\frac{\Omega_B^2 - \Omega^2}{\Omega^2 - \Omega_A^2}}\, k_z^i. \tag{35}$$

Eq. (34) is similar to Eq. (32). The left hand side is just $\cot(k_z^i S)$, as before. The right hand side $G(\Omega)$ function is the same as the second form of the $F(\Omega)$ function of Eq. (32), except that Ω_A appears in place of Ω_H and there is an additional $-\sin^2\phi$ term in the numerator. Eq. (35) is the same as Eq. (33), but with Ω_A in place of Ω_H. These similarities lead to dispersion solutions for the various branches which have more-or-less the same overall character as shown in Fig. 3, except that the lower frequency band limit at $\Omega = \Omega_H$ for $\phi = 0°$ is replaced with Ω_A. This Ω_A bottom limit moves up as the propagation angle increases, as shown in Fig. 2.

There is also one very important difference in the dispersion solutions for nonzero propagation angles which stems from the extra $\sin^2\phi$ term in Eq. (34). Recall that for the backward volume mode case at $\phi = 0°$, the right hand side of Eq. (32) diverges to $-\infty$ at the lower band limit Ω_H and diverges to $+\infty$ at the upper band limit Ω_B. The corresponding divergence to $-\infty$ at Ω_A is also true for $\phi \neq 0°$. However, the divergence to $+\infty$ at Ω_B is now true

only if ϕ is *below* some critical value. It is clear from Eq. (34) that if the condition

$$\sin^2\phi > \left(\Omega^2 - \Omega_A^2\right) \tag{36}$$

is satisfied, the divergence at the upper band limit $\Omega \to \Omega_B$ will be to $-\infty$, the *same* as for the Ω_A band limit. This change has a dramatic effect on both the nature of the dispersion curves for the various branch solutions, particularly the lowest order branch, and on the mode profiles. It is clear, for example, that if the divergences at both frequency band limits are negative, the limiting values of $k_z^i S$ for a given branch index n will be the same at these limiting frequency points and equal to $n\pi$. This means, among other things, that the lowest order $n = 1$ branch no longer evolves into the uniform mode at $k = 0$, but into a standing mode with one-half wavelength across the film thickness and $k_z^i S = \pi$. This change also causes the lowest order $n = 1$ Ω vs. k dispersion curve to have zero slope in the $k = 0$ limit.

The smallest value of ϕ which satisfies the condition of Eq. (36) defines a critical angle ϕ_c:

$$\phi_c = \tan^{-1}\sqrt{\Omega_H}\,. \tag{37}$$

For the YIG parameters used above, one obtains $\phi_c = 37.1°$. This is the same critical angle indicated in Fig. 2 for the emergence of the surface mode band. It is usually associated with the emergence of the nonreciprocal surface mode in the DE theory. The above results clearly show that this critical angle plays a key role for the volume modes as well. The critical angle effect for the volume modes is not widely realized.

Fig. 5 shows a series of dispersion curve diagrams for five values of the propagation angle ϕ, at $\phi = 0°$, 30°, 45°, 60°, and 90°, and the same YIG parameters used for Figs. 2, 3 and 4. The two smaller angles are below and the three larger angles are above the critical angle ϕ_c. As in Fig. 4, the dispersion curves are of reduced frequency Ω vs. reduced wave number kS, and they are based on the same field and YIG saturation induction values used for Figs. 2 and 3. Each diagram shows three volume mode dispersion curves, labeled V1, V2, and V3, as indicated. These curves correspond to the three lowest dispersion branches with indices $n = 1$, 2, and 3, respectively. The three diagrams for $\phi > \phi_c$ also show the surface mode dispersion branch, labeled S. The upper and lower volume mode band frequency limits Ω_B and Ω_A, and the upper surface mode limit frequency Ω_S, are shown in each diagram by the horizontal dotted lines. The surface mode aspects of Fig. 5 will be discussed later. The focus, for now, is on the volume mode properties.

The diagrams in Fig. 5 demonstrate the basic volume mode dispersion features discussed above. As ϕ increases from 0° to 90°, the bottom volume mode band limit frequency Ω_A moves up to meet Ω_B, the same as shown in Fig. 2. In the limit

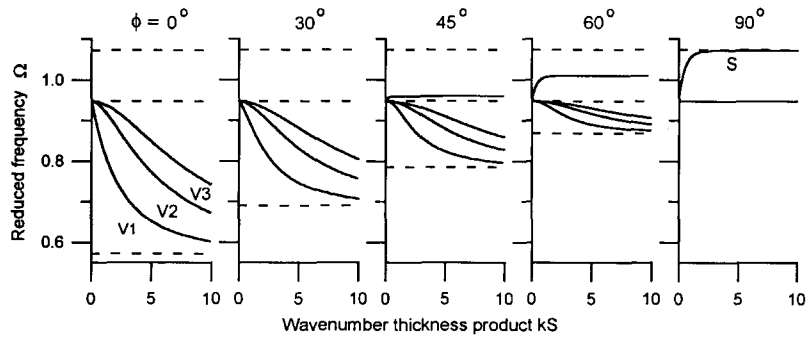

Fig. 5. Dispersion curves of reduced frequency Ω vs. reduced wavenumber kS for five values of the propagation angle ϕ, as indicated. Each diagram shows three curves labeled V1, V2, and V3 which correspond to the three lowest order volume mode dispersion branches. The diagrams for $\phi > \phi_c = 37.1°$ also show the surface mode dispersion curve, indicated by the S label. The upper and lower volume mode band limit frequencies Ω_B and Ω_A, and the upper surface mode band limit frequency Ω_S, are shown in each diagram by the horizontal dotted lines. All curves are based on values for the static in-plane field H_0 and the film saturation induction $4\pi M_s$ of 1000 Oe and 1750 G, respectively, as for Fig. 4.

$\phi \to 90°$, moreover, the volume mode band collapses to zero width as all of the volume mode dispersion branches merge together into one horizontal line at $\Omega = \Omega_B$. Strictly speaking, however, there can be no volume modes at $\phi = 90°$ and $\Omega = \Omega_B$ except at $k = 0$. This result is evident from Eq. (35)

The diagrams in Fig. 5 also show that the lowest order volume mode dispersion curve has an initial slope at $kS = 0$ which is nonzero for the ϕ-values below the critical angle $\phi_c = 37.1°$ and an initial slope of zero for ϕ-values above ϕ_c. As will be shown in the next section, concurrent with the change in character for lowest order volume mode at $\phi = \phi_c$, a new dispersion branch emerges from the top of the volume mode band at Ω_B. In the $kS \to 0$ limit, this new surface mode reduces to the uniform mode. This new mode also has a nonzero and positive Ω vs. kS slope at $kS = 0$, and evolves with a nonreciprocal surface character with increasing kS. In effect, when ϕ exceeds ϕ_c, this surface branch becomes the lowest order mode which has a uniform mode profile in the $kS = 0$ limit, and the initial lowest order volume mode becomes the second order mode with a standing wave $k_z^i S = \pi$ character at $kS = 0$. The corresponding surface mode dispersion curves are shown in Fig. 5. The surface mode is discussed in Section 5.

4. Volume mode polarizations and profiles

Turn now to a consideration of mode polarizations and profiles for the volume modes. It is important to note at the outset that the trial functions specified by Eqs. (7)–(14) correspond to scalar potentials inside and outside the film. For a given branch at a Ω-value, k-value, and ϕ-value, $k_z^i S$ is specified and $k_z^e = k$ is also specified. From Eqs. (7), (9)–(12), and (19)–(21), the total scalar potential inside the film, $\psi^i(\boldsymbol{r})$, is then obtained and is completely specified within some multiplicative factor. Most past treatments of DE mode profiles have considered only the z-dependence for $\psi^i(\boldsymbol{r})$, through the $Z^i(z)$ function as defined by Eqs. (12) and (19)–(21). However, in order to obtain a physical picture of the modes, it is necessary to calculate profiles for the y- and z-components of the *dynamic magnetization* $\boldsymbol{m}$ across the film cross section. These magnetization profiles are discussed only briefly by Sparks [21].

Recall that the formulation so far is for a complex $\boldsymbol{h}(\boldsymbol{r},t)$ and $\boldsymbol{m}(\boldsymbol{r},t)$, given in component form as $h_{y,z}(\boldsymbol{r},t) = h_{y0,z0}(z)\exp(i[\boldsymbol{k}\cdot\boldsymbol{r} - \omega(k)t])$ and $m_{y,z}(\boldsymbol{r},t) = m_{y0,z0}(z)\exp(i[\boldsymbol{k}\cdot\boldsymbol{r} - \omega(k)t])$. The field amplitudes associated with a given mode derive from the $Z^i(z)$ functions for that mode according to $h_{y0}(z) = ikZ^i(z)\sin\phi$ and $h_{z0}(z) = dZ^i(z)/dz$. The complex magnetization amplitudes m_{y0} and m_{z0} are then obtained from the connection between $\boldsymbol{h}$ and $\boldsymbol{m}$ through the κ and ν parameters according to Eqs. (2)–(6). In order to examine polarization properties and actual response profiles as a function of z, it is necessary to consider the real dynamic magnetization response. From the formalism developed above, the real dynamic magnetization response at $x = y = 0$ may be written as $\mathrm{Re}[4\pi m_y(z,t)] = 4\pi m_{y0}(z)\sin(\omega t)$ and $\mathrm{Re}[4\pi m_z(z,t)] = 4\pi m_z^0(z)\cos(\omega t)$, where $4\pi m_y^0(z)$ and $4\pi m_z^0(z)$ are real:

$$\mathrm{Re}\left[4\pi m_y(z,t)\right] = 4\pi m_y^0(z)\sin(\omega t) = \left[+\kappa Z^i(z)k\sin\phi - \nu\frac{dZ^i(z)}{dz}\right]\sin(\omega t) \tag{38}$$

and

$$\mathrm{Re}\left[4\pi m_z(z,t)\right] = 4\pi m_z^0(z)\cos(\omega t) = \left[-\nu Z^i(z)k\sin\phi + \kappa\frac{dZ^i(z)}{dz}\right]\cos(\omega t). \tag{39}$$

The square bracket terms in Eqs. (38) and (39) correspond to the real amplitude parameters for the dynamic magnetization response. Note that these terms may be positive or negative. For the precession of $\boldsymbol{m}$ in a Larmor sense, as expected from Eq. (1), these terms should have opposite signs.

While the dynamic magnetization response given above has a fairly simple form, the square bracket expressions show that the connection between the scalar potential profile $Z^i(z)$ and dynamic magneti-

zation profiles is far from simple. This connection involves both $Z^i(z)$ and the z-derivative of $Z^i(z)$. Recall that $Z^i(z)$ contains both $\sin(k_z^i z)$ and $\cos(k_z^i z)$ terms. Each dependence will be weighted in a way which depends on the propagation direction and the frequency, and will in general be different for both of the two transverse components of the dynamic response. Recall also that the κ and ν parameters from the susceptibility tensor defined through Eqs. (2)–(4) depend on the frequency Ω and the band limit frequencies Ω_B and Ω_H as well. It is clear why past workers have been content with an examination of the much simpler $Z^i(z)$ profiles. However, results given below for dynamic magnetization profiles reveal much more symmetry, and much more physical significance.

One important and little appreciated property of the volume modes is immediately apparent from the form of Eqs. (38) and (39). Each equation contains two terms, one with a $k\sin\phi$ multiplier and one with no explicit k terms. This means that for modes for which ϕ is nonzero, the mode profiles will be nonreciprocal. That is, the profiles for one sign of ϕ will be different from the profiles for ϕ of the opposite sign. The numerical results shown below will bear out this observation. The nonreciprocal properties for the surface mode, to be considered in the next section, are well known. The fact that the volume modes also have nonreciprocal properties is not widely realized.

Before considering actual profiles, and as a check on the physical nature of the dynamic magnetization response, it is useful to examine the polarizations and ellipticities implicit in the response formulae given above. Simple analytical expressions are possible for the specific case of propagation in the x-direction, with $\phi = 0°$ and $k_y = 0$. In this case, one obtains

$$4\pi m_y^0(z) = -\nu \frac{dZ^i(z)}{dz} \tag{40}$$

and

$$4\pi m_z^0(z) = +\kappa \frac{dZ^i(z)}{dz}. \tag{41}$$

For the volume mode band, with $\Omega_H < \Omega < \Omega_B$, κ and ν from Eqs. (3) and (4) are both negative. It is clear, therefore, that $\phi = 0°$ modes are polarized in the Larmor sense with a counterclockwise rotation of $\boldsymbol{m}$ in the y–z plane. As will be evident from the numerical results given below, this property carries over to all branches for other propagation directions as well.

The ellipticity of the mode precession may be specified in terms of the $|m_y^0|/|m_z^0|$ ratio, $|\nu/\kappa|$. Since ν/κ is just Ω/Ω_H, it is also clear that these modes are elliptically polarized with the major axis in the film plane and along $\boldsymbol{e}_y$. In the limit of zero wave number, the mode frequency is Ω_B, and the $|m_y^0|/|m_z^0|$ ratio is Ω_B/Ω_H, the same as for ferromagnetic resonance. In the $k = \infty$ limit, with $\Omega = \Omega_H$, the $|m_y^0|/|m_z^0|$ ratio for these modes is unity and the modes are circularly polarized. This is as one would expect for spin waves propagating parallel to the static field, at the bottom of the volume mode band, and with $kS \gg 1$. It is shown below that the surface mode, at $\phi = 90°$ and in the short wavelength $kS \gg 1$ limit, is also circularly polarized. This situation is in considerable contrast with the present $\phi = 0°$ volume mode case, in that the mode frequency is above the usual volume mode band. The surface mode will be considered shortly.

Turn now to actual volume mode profiles. The square bracket expressions in Eqs. (38) and (39) for $4\pi m_y^0(z)$ and $4\pi m_z^0(z)$ give the z-dependent response functions for the dynamic magnetization components which correspond to the various dispersion curve branches discussed above. Fig. 6 shows representative sets of profiles from explicit numerical calculations for a range of propagation directions. The calculations are for YIG film material parameters and an in-plane x-directed static magnetic field of 1000 Oe. Fig. 6(a) is for the lowest order volume mode branch dispersion curve with $n = 1$. Fig. 6(b) is for the second, $n = 2$ branch. In each case, sets of profiles are shown for six different propagation directions, with ϕ increasing from the bottom profiles to the top profiles. The two lowest sets are for $\phi = 0°$ and $\phi = 25°$. The next three sets are for ϕ-values of 36°, 37.1°, and 38°, slightly below, precisely at, and slightly above ϕ_c. The top set is for $\phi = 60°$, well above ϕ_c. From left to right, the profiles in each set correspond to increasing values of kS. The left-most profiles are for $kS = 0.001$, to approximate the condition for zero wave number k.

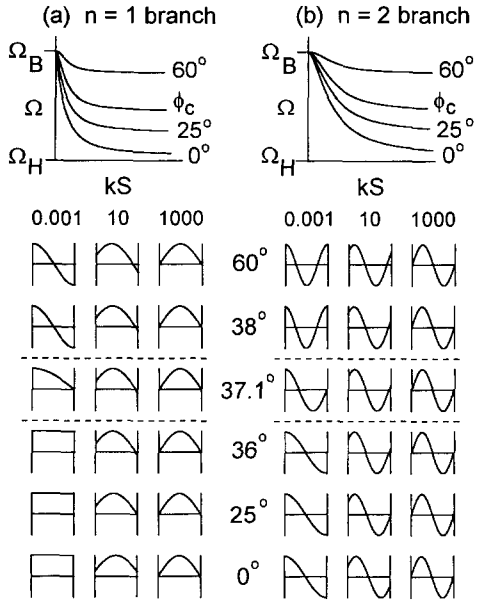

Fig. 6. Dispersion curves of reduced frequency Ω vs. reduced wavenumber kS and sets of dynamic magnetization mode profiles for $m_y^0(z)$ as a function of position z across the film for (a) the $n=1$ and (b) $n=2$ volume mode dispersion branches and six different values of in-plane propagation angle ϕ, as indicated. All curves are based on values for the static in-plane field H_0 and the film saturation induction $4\pi M_s$ of 1000 Oe and 1750 G, respectively, as for Fig. 4. The three $m_y^0(z)$ profiles in each set, from left to right, are for kS values of 0.001, 10, and 1000, respectively. From bottom to top, the dispersion curves and profiles in each set are for ϕ-values of 0°, 25°, 36°, 37.1°, 38°, and 60°. For consistent display, all profiles are scaled to a common peak value and shown with positive values at the left $z=-S/2$ side of the film.

This low $kS=0.001$ value also corresponds to the top of the band at $\Omega \approx \Omega_B$. The center column of profiles in each set is for $kS=10$, representative of mode shapes for intermediate kS values. The right-most column of profiles in each set is for $kS=1000$, representative of mode shapes for very large kS. The (a) and (b) profile sets in Fig. 6 are accompanied by sets of $n=1$ and $n=2$ dispersion diagrams, as shown at the top of the figure. These diagrams are included to provide dispersion reference points for the evolution in mode profile with increasing kS at a given propagation angle ϕ, and for the various propagation angles as well.

Each profile diagram in Fig. 6 shows a $4\pi m_y^0(z)$ profile curve only. The individual profile curves were obtained from numerical evaluations of the square bracket expression in Eq. (38) as a function of z over the range from $z=-S/2$ to $z=+S/2$. The left-most side of each profile corresponds to $z=-S/2$ and the right-most side to $z=+S/2$. The profiles are all scaled to a common maximum amplitude and shown with positive values at the left, $z=-S/2$ side of the film. Where a choice is necessary, the response at $z=-S/2$ is taken as positive. In order to keep these diagrams as simple as possible, the $m_z^0(z)$ profile curves are not shown. The m_z^0 profiles were generally smaller than the m_y^0 profiles and were of opposite sign. The smaller values reflect the ellipticity of the classical magnetization precession for in-plane magnetized films. The opposite sign corresponds to the expected Larmor sense of precession for the normal mode response.

Fig. 6 contains a large amount of information on the physical nature of the Damon–Eshbach volume modes, a significant part of which is generally not known, even to specialists in the subject. The problem here, as noted above, is that most past workers have been content to examine only the behavior of the scalar potential profiles, without considering the somewhat more involved algebra for the actual dynamic magnetization response. As evident from Fig. 6 and the discussion below, the actual $m_y^0(z)$ profiles show many new and unrealized effects.

Consider first the set of (a) profiles in Fig. 6 forthe lowest order $n=1$ dispersion branch. The profile diagrams show the evolution in $k_z^i S$ as kS increases from near zero to large values, already discussed in connection with the dispersion solutions. When the propagation angle is below the critical angle ϕ_c, the profiles evolve from uniform mode profiles with $k_z^i S=0$ at very low kS into harmonic standing wave profiles with $k_z^i S=\pi$ at very high kS. When the propagation angle is above the critical angle ϕ_c, the profiles start with harmonic standing wave character with $k_z^i S=\pi$ at very low kS, change somewhat in the intermediate range of kS values, and then revert back to pure harmonic standing waves with $k_z^i S=\pi$ again at very high kS. Precisely at the critical angle, the standing wave mode at low kS has $k_z^i S=\pi/2$. These limiting values of $k_z^i S$ are the same as obtained above in connection with the $n=1$ dispersion solutions. These values follow from the behavior of the $G(\Omega)$ function in the limits $\Omega \to \Omega_B$ for low kS and $\Omega \to \Omega_A$

for high kS and the various $\cot(k_z^i S)$ intersection points already discussed in connection with Fig. 3.

With respect to the mode profiles, however, there are two new results of note. The first of these concerns pinning. The (a) profiles in Fig. 6 show that with increasing kS, the $n = 1$ mode changes from a profile with *antinodes* at the film surfaces for very low kS into a standing wave mode profile with *nodes* at the film surfaces for very large kS. It is important to realize that these changes are not boundary condition effects. The initial boundary value problem did not involve any specific boundary conditions on the dynamic $\boldsymbol{m}$ response at the film surfaces. The only boundary conditions concerned the usual continuity for the components of $\boldsymbol{h}$ tangential to the film surfaces and the component of $\boldsymbol{b}$ perpendicular to the surfaces. The mode profiles which come out of the analysis show characteristics usually associated with so-called 'unpinned' films at low kS and with 'pinned' films at high kS. The terms 'pinned' and 'unpinned' relate to the nature of the dynamic magnetization response at the film surfaces through surface anisotropy [27]. There are two limiting surface conditions: (1) When there is no surface anisotropy present, the dynamic magnetization at the film surfaces satisfies the condition $\mathrm{d}m^0_{y,z}(z)/\mathrm{d}z|_{z=\pm S/2} = 0$. (2) When the surface anisotropy energy is extremely strong relative to exchange, the dynamic magnetization at the film surfaces simply satisfies the condition $m^0_{y,z}(z)|_{z=\pm S/2} = 0$. In spite of the absence of such boundary conditions in the present problem, it is precisely conditions (1) and (2) which appear to be satisfied in the very low and very high kS limits for the Damon–Eshbach volume modes here. This effect will be termed *quasi-pinning*. This result for the volume magnetostatic modes in films and slabs is not widely realized. Further comments on quasi-pinning will be made at the end of this section.

The second new result here concerns nonreciprocal propagation. The effect is the most pronounced for propagation precisely at the critical angle and at low kS. Here, the mode profile has a maximum on the $z = -S/2$ surface and a zero on the opposite $z = +S/2$ surface. In the terminology introduced above, this mode is quasi-unpinned on the left side and quasi-pinned on the right side. The nonreciprocal property comes from the effect of changing the sign of the propagation angle ϕ. With $\phi = \phi_c = +37.1°$, the mode profile is as shown in Fig. 6. If ϕ is reversed in sign to $-37.1°$, the node and antinodes change sides. This means that for one sign of the propagation angle ϕ, the mode is associated more-or-less with one side of the film, and then flips to the other side when the sign of ϕ is reversed. Such nonreciprocal effects are generally well known for the surface mode. It is not widely realized that these effects are also present for the volume modes. In the limit of very large kS values, as for the right column of profiles in Fig. 6(a), the modes are quasi-pinned and entirely symmetric. For the intermediate range of kS values represented by the middle column of profiles, one sees some degree of nonreciprocal behavior for all propagation angles except at $\phi = 0°$.

The mode profile results discussed so far, and in conjunction with Fig. 6(a), have been for the lowest order $n = 1$ dispersion branch. These same results carry over to the higher order dispersion branches as well. Fig. 6(b) shows profiles for the second, $n = 2$ branch. The format is the same as for Fig. 6(a). These profile diagrams also show the expected evolution in $k_z^i S$ as kS increases from near zero to large values, already discussed in connection with dispersion. When the propagation angle is below the critical angle ϕ_c, the profiles evolve from standing mode profiles with $k_z^i S = \pi$ at very low kS into harmonic standing wave profiles with $k_z^i S = 2\pi$ at very high kS. When the propagation angle is above the critical angle ϕ_c, the profiles start with harmonic standing wave profiles with $k_z^i S = 2\pi$ at very low kS, change somewhat in the intermediate range of kS values, and then revert back to pure harmonic standing wave profiles with $k_z^i S = 2\pi$ again at very high kS. Precisely at the critical angle, the standing wave mode at low kS has $k_z^i S = 3\pi/2$. These limiting values of $k_z^i S$ are the same as obtained in connection with the $n = 2$ dispersion solutions and follow from the behavior of the $G(\Omega)$ function in the limits $\Omega \to \Omega_B$ for low kS and $\Omega \to \Omega_A$ for high kS and the various $\cot(k_z^i S)$ intersection points already discussed in connection with Fig. 3.

In addition to these expected features, the $n = 2$ branch profiles also show the quasi-pinning and nonreciprocal propagation effects just noted for the $n = 1$ dispersion branch. At high kS, all modes are quasi-pinned at the film surfaces, regardless of the propa-

gation angle ϕ. Except for propagation just at the critical angle, the profiles are all quasi-unpinned at low kS. For propagation just at the critical angle, the mode profile at low kS is quasi-pinned on one side and quasi-unpinned on the other side. The mode at $\phi = \phi_c = +37.1°$ and $kS = 0.001$ in Fig. 6(b) is somewhat more localized near the left side of the diagram than the right side. If ϕ is changed to $-37.1°$, the profile flips. Nonreciprocal behavior, albeit not particularly pronounced, is also evident for all propagation angles except at $\phi = 0°$ for the middle column of profiles at $kS = 10$ in Fig. 6(b).

As was evident from the discussion of dispersion curves and the results in Fig. 5, it is very clear that there are very significant changes in the nature of the lowest order dispersion branch and its associated mode profiles when the propagation angle moves from below to above the critical angle ϕ_c. The results in Fig. 5 show that the initial slope of the dispersion change from nonzero to zero. The results in Fig. 6 show that one loses the uniform mode response completely, and that the uniform mode profile converts into a quasi-unpinned standing wave pattern with $k_z^i S = \pi$. As will be discussed in the next section, the uniform mode is not lost in this theory, but simply reemerges as the limiting case of a surface mode. Fig. 6 also shows that as the lowest order volume mode branch loses its uniform mode character at low kS, it does not simply assume the character of the $n = 2$ dispersion branch for $\phi < \phi_c$. This is clear from a simple comparison of the bottom set of profiles in Fig. 6(b) with the top set of profiles in Fig. 6(a). While these profiles are identical for $kS = 0.001$, they are totally different at $kS = 1000$. The $n = 2$ profile at $\phi = 0°$ and $kS = 1000$ has odd symmetry relative to the film center and $k_z^i S = 2\pi$. The $n = 1$ profile at $\phi = 60°$ and $kS = 1000$ has even symmetry and $k_z^i S = \pi$. The diagrams show that the $n = 2$ profiles at low kS goes from odd symmetry relative to the film center for $\phi < \phi_c$ to even symmetry for $\phi > \phi_c$. The $n = 1$ profiles at low kS goes from the uniform mode and even symmetry for $\phi < \phi_c$ to odd symmetry for $\phi > \phi_c$. It is clear, therefore, that the disappearance of the uniform mode limit from the volume mode solutions for $\phi > \phi_c$ causes the properties of *all* of the volume mode branches to change, not just the $n = 1$ branch. The most apparent change, of course, is in the change in slope for the $n = 1$ branch from nonzero to zero. As is evident from this discussion and the profiles in Fig. 6, there is also a change in profile evolution and profile symmetry for all branches.

Return now to the matter of quasi-pinning. The quasi-unpinned nature of the modes for very low kS is not particularly disturbing. This is due to the fact that most magnetic films are of high quality, and such YIG films as used in most experiments do in fact satisfy the unpinned film condition $dm_{y,z}^0(z)/dz|_{z=\pm S/2} = 0$. However, there are films of good quality which have high surface anisotropy. The magnetostatic modes for such films must satisfy, therefore, the condition $m_{y,z}^0(z)|_{z=\pm S/2} = 0$. The present results and the quasi-unpinned profiles for $kS = 0.001$ in Figs. 6(a) and (b) indicate that the DE theory is of limited applicability to the low kS modes in such films. The reverse conclusion is valid at high kS. Here, the predominance of quasi-pinned profiles from the DE theory indicate that the analysis should be applicable to pinned films and not to unpinned films. If one takes $kS = 10$ as a rule of thumb for the boundary between the regions of applicability for the DE theory, and considers a YIG film with $S = 10$ μm, one obtains a cut-off wave number of $k \approx 10^4$ cm^{-1}. This means that the DE theory is applicable to unpinned films for $k \leq 10^4$ cm^{-1} and to pinned films for $k \geq 10^4$ cm^{-1}. It is to be emphasized that this is not a rigorous cutoff condition. It is only a statement that the normal modes from the DE theory provide a reasonable match to the normal modes of a real film when this limit on k is satisfied.

In closing this section, it is to be noted that this problem of quasi-pinning for the volume magnetostatic modes is a pathological effect which stems from the neglect of exchange in the theory. It is well known that exchange is important for very large k-values in excess of 10^5 cm^{-1} and for films thinner that 1 μm or so. The basic effect is an additional k^2 term for the dispersion curves given above and an upward frequency shift for the various dispersion branches at $k = 0$ which scales as n^2. These effects also result in various branch dispersion crossings and interactions which give rise to a more complex array of so-called dipole exchange spin waves than evident from the magnetostatic formalism given above.

These frequency shifts due to exchange may be large or small, and will give correspondingly large or

small changes in mode frequencies. The more important effect of exchange, in the present context, is in the additional equations and the need to include boundary conditions on $\boldsymbol{m}_0(z)$ at the film surfaces in the analysis. When exchange is included in the formal theory, one may also include bonafide boundary conditions on the dynamic magnetization at the film surfaces, following the initial work of Rado and Weertman [27]. This leads to modes with a well defined pinning character at the film surfaces which does not change with kS. A full discussion of pinning effects and their importance for magnetic excitations in thin films is beyond the scope of this work. It is sufficient to note that the actual boundary conditions on the dynamic magnetization at the film surfaces are fully defined by the physical properties of the film surfaces, and do not change with wave vector. Such boundary conditions can only be accommodated with the inclusion of exchange in the analysis and by a full treatment of the so-called dipole-exchange modes of the structure. Details of the analysis procedure for such modes are contained in numerous papers by Sparks [21], DeWames and Wolfram [22], Wolfram and DeWames [23], Kalinikos [24], and Kalinikos and Slavin [25]. The implication in the present context is that actual profiles for the dynamic modes of the film should show an evolution with increasing kS which is rather different from the patterns shown in Fig. 6. It is perhaps remarkable that the basic dispersion curves predicted from magnetostatic theory are well corroborated by many experiments [7,8], in spite of the fundamental problem in the theory for the actual mode profiles. The pathology inherent in the DE theory should be readily apparent for pinned films at low kS values below 10 or so, or for unpinned films at kS above 10.

5. Damon–Eshbach surface mode

The discovery of a nonreciprocal propagating mode with surface character was one of the most important results of the original analysis done by Damon and Eshbach. The surface mode can occur, in the context of the formalism given above, if the k_z^i parameter is imaginary. Recall that there was no a priori reason in the formalism for k_z^i to be real. Consider the effect on the scalar potential z-dependence if k_z^i is written as

$$k_z^i = i\kappa_z^i, \tag{42}$$

where κ_z^i is real. Substitution of k_z^i in this form into Eq. (12) leads to a scalar potential $Z^i(z)$ function of the form

$$Z^i(z) = a' e^{+\kappa_z^i z} + b' e^{-\kappa_z^i z}, \tag{43}$$

where the coefficients a' and b' are given in terms of the a and b coefficients as $a' = (b + ia)/2$ and $b' = (b - ia)/2$. The exponential z-dependences for the $Z^i(z)$ function in Eq. (43) lead to a mode profile with a surface character. This result will be considered shortly.

It is first necessary, however, to examine the conditions under which imaginary k_z^i and real κ_z^i solutions are possible. If k_z^i is replaced by $i\kappa_z^i$ in Eq. (23), one obtains

$$\kappa_z^i = \mp \sqrt{\frac{1 + \kappa \sin^2\phi}{1 + \kappa}}\, k. \tag{44}$$

The main difference between Eq. (44) and Eq. (23) is the absence of the negative sign *inside* the square root. In the previous two sections, it was the requirement that the square root argument with a negative sign be positive that led to the $\Omega_B > \Omega > \Omega_A$ frequency condition for the volume modes just discussed. For this same expression without the negative sign to be positive, the condition on frequency becomes $\Omega > \Omega_B$ or $\Omega < \Omega_A$. This means that the surface mode is possible, in principle, for all frequencies outside the volume mode band. As will be evident shortly, however, the frequency limits for the surface mode are much more restrictive than implied from Eq. (44) alone. The surface mode is allowed for a small band of frequencies just above $\Omega = \Omega_B$.

The next step in the surface mode analysis is to rewrite Eq. (22) in terms of κ_z^i rather than k_z^i, and construct terms which apply explicitly to the applicable $\Omega < \Omega_A$ or $\Omega > \Omega_B$ range of frequencies outside the volume mode band. The $k_z^e = k$ condition of Eq. (24) is still applicable. One constructs appropriate counterparts to Eqs. (34) and (35) based on the $i\kappa_z^i$ replacement, Eq.(44), and the explicit expressions for κ and ν defined through Eqs. (3)–(6). The

$k_z^e = k$ and $k_z^i = i\kappa_z^i$ replacements in Eq. (22) yield

$$k^2 + (\kappa_z^i)^2(1+\kappa)^2 - \nu^2 k^2 \sin^2\phi + 2k\kappa_z^i(1+\kappa)\coth(\kappa_z^i S) = 0. \quad (45)$$

The same remarks concerning the sign of k_z^i in connection with Eq. (22) apply here to κ_z^i. Neither the z dependence in the scalar potential, defined through the $Z^i(z)$ function in Eq. (12) and the various coefficients in Eqs. (19)–(21), nor the dispersion condition of Eq. (22), are affected by a change in sign for κ_z^i. In the surface analysis to follow, under conditions for which the square root argument in Eq. (44) is positive, κ_z^i will be taken as positive.

At this point, as for the volume modes, one proceeds to incorporate explicit expressions for κ and ν defined through Eqs. (3)–(6) to obtain Eq. (34) and Eq. (35) counterparts. The key difference from the previous calculation procedure for the volume mode band is that there are now two different frequency regimes which must be considered separately, one for the above band case $\Omega > \Omega_B$ and one for the below band case $\Omega < \Omega_A$. For both cases, the counterpart to Eq. (35) is the same and is given by

$$k = \sqrt{\frac{\Omega^2 - \Omega_B^2}{\Omega^2 - \Omega_A^2}}\,\kappa_z^i. \quad (46)$$

The counterpart equation to Eq. (34), however, is different for $\Omega > \Omega_B$ and $\Omega < \Omega_A$. This is due to the details of the manipulations involving the $\kappa_z^i(1+\kappa)$ factor in the last term on the left hand side of Eq. (45). The correct evaluation of this factor involves the combination of $(\Omega^2 - \Omega_B^2)$ terms which occur both inside and outside the square root, and a $(\Omega^2 - \Omega_B^2)$ term inside the square root. It is necessary to write these terms as explicitly positive to obtain the correct dispersion equation counterparts to Eq. (34). In the below band case, $\Omega < \Omega_A$, one obtains

$$\coth(\kappa_z^i S) = H(\Omega) = -\frac{1}{2}\left[\frac{\sin^2\phi + (\Omega_B^2 - \Omega^2) + (\Omega_A^2 - \Omega^2)}{\sqrt{(\Omega_B^2 - \Omega^2)(\Omega_A^2 - \Omega^2)}}\right] \quad (\Omega < \Omega_A), \quad (47)$$

In the above band case for $\Omega > \Omega_B$, one obtains

$$\coth(\kappa_z^i S) = I(\Omega) = \frac{1}{2}\left[\frac{\sin^2\phi + [(\Omega^2 - \Omega_A^2) - (\Omega^2 - \Omega_B^2)]}{\sqrt{(\Omega^2 - \Omega_B^2)(\Omega^2 - \Omega_A^2)}}\right] \quad (\Omega > \Omega_B). \quad (48)$$

Note that all terms in Eqs. (47) or (48) which involve differences between Ω^2 and Ω_A^2 or Ω_B^2 are written in explicitly positive form. Recall as well that κ_z^i is taken as positive and that Ω_B is greater than Ω_A. In the limit $\phi \to 90°$, Ω_A approaches Ω_B from below.

The final step in the surface mode dispersion analysis is to consider solutions to Eqs. (47) and (48). It is evident from Eq. (47) that there is no below band surface mode. The left hand side of Eq. (47) is always positive and the right hand side is always negative. The surface mode, if present, will appear above the volume mode frequency band only and satisfy the dispersion relation implicit in Eq. (48). In contrast with the volume mode dispersion condition in Eq. (34) involving $\cot(k_z^i S)$ and multiple branches, the $\coth(\kappa_z^i S)$ function in Eq. (48) has only a single branch. It is only necessary to consider the limitations imposed by the right hand side $I(\Omega)$ function, in combination with Eq. (46), to determine the surface mode dispersion characteristics. Recall that $\coth(u)$ is simply $(e^u + e^{-u})/(e^u - e^{-u})$. With u positive, this function diverges to $+\infty$ as u approaches 0 and approaches 1 as u goes to ∞. Applied to Eq. (48), this means than in the limit $\Omega \to \Omega_B$, the divergence caused by the $(\Omega^2 - \Omega_B^2)$ term in the denominator corresponds to $\kappa_z^i S \to 0$. As the frequency is increased from this lower Ω_B limit, the value of the $I(\Omega)$ function will decrease. The point in frequency at which $I(\Omega)$ drops below unity will determine the upper cutoff frequency limit for the single surface mode band, and this frequency limit will correspond to $\kappa_z^i S = \infty$. The condition $I(\Omega) = 1$, therefore, determines the upper limit surface mode frequency Ω_U at a given propagation angle ϕ. This upper limit surface mode frequency is obtained as

$$\Omega_U^2 = \Omega_B^2 + \frac{(\sin^2\phi - \Omega_H \cos^2\phi)^2}{4\sin^2\phi}, \quad (49)$$

subject to the condition

$$\phi > \phi_c = \tan^{-1}\sqrt{\Omega_H}\,. \tag{50}$$

Eq. (50) corresponds precisely to the critical angle condition already encountered for the volume modes. Recall that the volume mode dispersion curves change character at the critical angle ϕ_c and the uniform mode profile for the $n = 1$ volume mode branch in the $k_z^i S \to 0$ and $\Omega \to \Omega_B$ limit *disappears* for $\phi > \phi_c$. The above analysis shows that as the volume mode branch associated with the uniform mode disappears for $\phi > \phi_c$, a new surface dispersion branch emerges. This branch, moreover, has the uniform mode character with $\kappa_z^i S = 0$ in the $\Omega \to \Omega_B$, $k \to 0$ limit. As is evident from Eq. (49), this surface dispersion branch collapses to a single frequency at $\Omega = \Omega_B$ in the limit $\phi \to \phi_c$. For $\phi > \phi_c$, the dispersion curve extends to frequencies above Ω_B as the wave number k increases and reaches the upper frequency limit Ω_U for $kS \gg 1$. In the limit of propagation perpendicular to the static field and magnetization direction corresponding to $\phi = 90°$, one obtains a single branch surface mode band with Ω in the range $\Omega_B < \Omega < [\Omega_H + 1/2]$. The upper limit frequency at $\phi = 90°$ is often called the Damon–Eshbach surface mode frequency Ω_S:

$$\Omega_S = \Omega_H + \frac{1}{2}\,. \tag{51}$$

As in the volume mode case, one can proceed with the evaluation of surface mode dispersion curves and mode profiles by numerical methods. Some representative surface mode dispersion curves were shown and discussed briefly in connection with Fig. 5. The basis for these dispersion curves is now clear. The surface branch appears for propagation angles above ϕ_c. The surface mode frequency starts out at $\Omega = \Omega_B$ for $kS = 0$, increases rapidly with increasing kS, and levels off at the upper limit surface mode frequency Ω_U for values of kS on the order of unity or greater. With increasing ϕ, Ω_U also increases and reaches a maximum value at $\phi = 90°$. This maximum is indicated by the upper dashed line in Fig. 5. This maximum surface mode frequency corresponds to the Damon–Eshbach surface mode frequency, Ω_S.

The surface mode has a number of peculiar properties. First of all, it is noteworthy that the surface mode frequencies in general, and the Damon–Eshbach frequency Ω_S in particular, lie above the top of the spin wave band at low wave numbers implicit in Eqs. (30) and (31). It is somewhat surprising to obtain a normal mode spin wave frequency which is outside the usual spin wave band. This above-band Damon–Eshbach frequency, however, is closely related to spin wave considerations. It is well known that if one neglects the ellipticity of the spin precession when analyzing the spin wave dispersion, instead of Eq. (30), one obtains [34] a somewhat simpler dispersion equation of the form

$$\omega_k = \gamma\left(H_0 + Dk^2 + 2\pi M_s \sin^2\theta_k\right). \tag{52}$$

For propagation perpendicular to the static field at a spin wave propagation angle $\theta_k = 90°$ and small wave numbers so that exchange can be neglected, Eq. (52) gives a spin wave frequency identical to the Damon–Eshbach frequency in Eq. (51). The physical reasons for this equivalence are connected with the nature of the surface mode profile and polarization. These effects will be considered shortly.

Second, and as already indicated, the Damon–Eshbach surface mode is highly nonreciprocal. It is apparent from Eq. (43) that the rate of the exponential decay in the surface mode response is essentially controlled by κ_z^i. Further, Eq. (46) indicates that κ_z^i scales with the propagation wave number k. This means that as one goes to higher and higher values of kS, the mode profile decays more and more rapidly. As will be shown shortly, this decay starts at the film surface. This means therefore, that as kS increases, the response becomes more and more localized at the film surface. The amount of relative localization is roughly proportional to $1/kS$. For $kS = 10$, for example, the mode profile is localized in about $1/10$ of the film cross section near the surface. This localization, moreover, is at one rather than both surfaces. When ϕ has one sign, the localization is at one surface. When ϕ has the opposite sign, the localization is at the other surface. This is the basic nonreciprocal propagation property of interest here.

In parallel with the volume mode discussion, surface mode properties will be considered from two perspectives. First, the basic polarization and nonreciprocal properties indicated above will be examined from an analytical perspective. For this purpose, the

discussion will be limited to the special case of perpendicular propagation at $\phi = \pm 90°$ in the $kS \gg 1$, $\Omega \to \Omega_S$ limit. It will be demonstrated that the two opposite propagation directions at $\phi = \pm 90°$ corresponds to a surface mode which is localized at the bottom, $z = -S/2$, and top, $z = +S/2$, surfaces of the film respectively. It will also be shown that the nonreciprocal surface mode is circularly polarized. It is this circular polarization property that pushes the surface mode frequency above the top of the normally elliptically polarized spin wave volume mode band and yields a limiting frequency Ω_S which matches the top of the spin wave band in the zero ellipticity approximation. As a second perspective, mode dispersion curves and mode profiles will be evaluated numerically for a range of propagation angles and kS values. These results parallel the discussion for volume modes and the results of Fig. 6.

In the special case of perpendicular propagation at $\phi = 90°$, the surface mode dispersion has the form

$$\Omega^2 = \Omega_B^2 + \frac{1}{2 + 2\coth(\kappa_z^i S)}. \tag{53}$$

In the limit $\kappa_z^i S \to 0$, one obtains $\Omega \to \Omega_B$ from Eq. (53) and $k \to 0$ from Eq. (46). This is the uniform mode ferromagnetic resonance limit already discussed in connection with the lowest order $n = 1$ volume modes dispersion in the $k \to 0$ limit for propagation below the critical angle. In the $\kappa_z^i S \to \infty$ limit, one obtains $\Omega \to \Omega_S$ and $k \to \infty$. The 'S' curve in the right most diagram in Fig. 5 shows the basic shape of the surface mode dispersion curve specified by Eq. (53) with the same YIG parameters and field value used for the other curves.

The surface mode nonreciprocal and polarization properties may be obtained in simple analytic form for the case of perpendicular propagation in the high-$\kappa_z^i S$, high-kS, $\Omega \approx \Omega_S$ limit. In this limit, the connection between κ_z^i and k in Eq. (46) reduces to $\kappa_z^i = k$. The form of the internal scalar potential function $Z^i(z)$ also becomes rather simple in this Damon–Eshbach surface mode high kS limit. It is necessary to consider the two opposite propagation directions corresponding to $k_y = \pm k$ separately. The $k_y = +k$ case corresponds to propagation in the positive y-direction with $\phi = +90°$. The $k_y = -k$ case corresponds to propagation in the negative y-direction with $\phi = -90°$. With this $k_y = \pm k$ replacement, explicit expressions for κ and ν from Eqs. (3) and (4), the $k_z^e = k$ condition from Eq. (24), and the $k_z^i = i\kappa_z^i$ substitution from Eq. (42), along with the replacements $\cot(k_z^i S/2) = \coth(\kappa_z^i S/2) = 1$ and $\kappa_z^i = k$ which are valid in the $\Omega \to \Omega_S$ limit, Eq. (21) reduces to $(c - d)/(c + d) = \mp 1$. The internal scalar potential function $Z^i(z)$ then becomes, apart from factors common to both terms in Eq. (12),

$$Z^i(z) \propto \frac{\cosh(kz)}{\cosh(kS/2)} \mp \frac{\sinh(kz)}{\sinh(kS/2)} \quad (|z| < S/2). \tag{54}$$

The cosh and sinh functions may be written in terms of exponential arguments according to $\cosh(u) = (e^u + e^{-u})/2$ and $\sinh(u) = (e^u - e^{-u})/2$. This gives a $Z^i(z)$ function of the form

$$Z_\pm^i(z) \propto e^{+k(S/2 \mp z)} - e^{-k(S/2 \mp z)} \quad (|z| < S/2). \tag{55}$$

The upper and lower signs correspond to the $k_y = \pm k$ propagation conditions defined above. Recall that the above analysis is for the $\Omega \to \Omega_S$ limit for which $kS \gg 1$ is valid. In this limit, Eq. (55) gives a large value for $Z^i(z)$ at $z = -S/2$ and a zero value at $z = +S/2$ for propagation in the positive y-direction at $k_y = +k$. For propagation in the negative y-direction at $k_y = -k$, $Z^i(z)$ is large at $z = +S/2$ and zero at $z = -S/2$. Because kS is very large, the mode is essentially localized at the bottom $z = -S/2$ surface for positive k_y and at the top $z = +S/2$ surface for negative k_y. The $Z^i(z)$ functions, therefore, may be written in terms of simple exponential decay according to

$$Z_+^i(z) \propto e^{k(S/2 - z)} \quad (|z| < S/2, k_y = +k) \tag{56}$$

and

$$Z_-^i(z) \propto e^{k(S/2 + z)} \quad (|z| < S/2, k_y = -k). \tag{57}$$

Fig. 7 shows, in schematic form, the nonreciprocal nature of the propagation implicit in Eqs. (56) and (57), with the mode which is localized at the bottom surface of the film propagating in the positive y-direction and the mode which is localized at the top surface propagating in the negative y-direction. Fig. 7 does not represent actual profiles. In the applicable

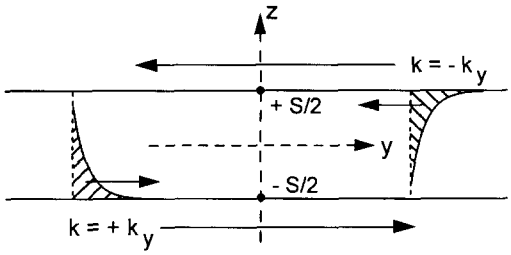

Fig. 7. Schematic profiles for the scalar potential $Z^{i}(z)$ functions which correspond to two nonreciprocal surface modes, one which is localized at the $z = -S/2$ film surface and propagating in the positive y-direction with $k_y = +k$, and one which is localized at the $z = +S/2$ film surface and propagating in the negative y-direction with $k_y = -k$.

$kS \gg 1$ limit, the actual profiles would much more localized at the film surfaces than shown in the diagrams. The nonreciprocity follows a right hand rule of sorts, in that the surface mode circulates around the positive x-direction and the direction of the static magnetic field $\boldsymbol{H}_0$ and the static saturation magnetization vector $\boldsymbol{M}_s$.

Turn now to the polarization properties for the dynamic magnetic field $\boldsymbol{h}(\boldsymbol{r},t)$ and dynamic magnetization $\boldsymbol{m}(\boldsymbol{r},t)$ associated with the two modes obtained above. The $Z^{i}_{\pm}(z)$ functions in Eqs. (56) and (56) yield an overall scalar potential given by $\psi^{i}_{\pm}(\boldsymbol{r}) = \exp[+k(S/2 \mp z)] \exp[\pm iky]$, where the upper and lower signs refer to propagation at $k_y = \pm k$, respectively. This $\psi^{i}_{\pm}(\boldsymbol{r})$, in combination with the $\boldsymbol{h}(\boldsymbol{r}) = \nabla\psi(\boldsymbol{r})$ connection and the $\exp[-i\omega t]$ time dependence from Section 2, yields real dynamic field components h_y and h_z given by

$$h^{\pm}_{y}(\boldsymbol{r},t) = -Cke^{k(S/2 \mp z)} \sin(ky \mp \omega t) \quad (|z| < S/2, k_y = \pm k) \tag{58}$$

and

$$h^{\pm}_{z}(\boldsymbol{r},t) = \mp Cke^{k(S/2 \mp z)} \cos(ky \mp \omega t) \quad (|z| < S/2, k_y = \pm k). \tag{59}$$

The parameter C represents some factor common to both responses. As before, the upper and lower signs refer to propagation at $k_y = \pm k$, respectively, and the bottom or top surface localization discussed above. It is clear from Eqs. (58) and (59) that the dynamic magnetic fields associated with both surface modes have circular polarization with rotation in the Larmor sense. From Eq. (2), one obtains real dynamic magnetization components m_y and m_z given by Eqs. (58) and (59) with an additional common factor of $(\kappa + \nu)$. The dynamic magnetization response associated with these surface modes, therefore, also have circular polarization with rotation in the Larmor sense.

As indicated at the beginning of this discussion, this circular precession in the Larmor sense is the physical basis for surface mode frequencies which are above the top of the conventional bulk spin wave band. If ellipticity is neglected, low wave number spin waves propagating perpendicular to the direction of the static magnetic field $\boldsymbol{H}_0$ and the static saturation magnetization vector $\boldsymbol{M}_s$ have a frequency at the Damon–Eshbach frequency $\Omega_S = \Omega_H + 1/2$ [30]. If the full effect of the dipole fields in producing elliptical polarization for the spin precession is then included in the analysis, the spin wave frequencies decrease from Ω_S to Ω_B. In the case of Damon–Eshbach surface waves at $\phi = 90°$ and large kS, there is a compensation between the effect of the dipole fields associated with the propagation in the y-direction and the effect of the dipole field associated with the z-direction decay into the film. The result is a circularly polarized mode at a frequency Ω_S which is above the top of the bulk spin wave band.

It is useful to consider the effect of forcing these modes to be localized on the opposite surfaces. This is easily accomplished by writing $\psi^{i}_{\pm}(\boldsymbol{r})$ in the form $\psi^{i0}_{\pm}(\boldsymbol{r}) = \exp[+k(S/2 \pm z)] \exp[\pm iky]$. It is easy to show, following the same procedure as outlined above, that the surface waves which correspond to $\psi^{i0}_{\pm}(\boldsymbol{r})$ will have dynamic fields and magnetizations which are circularly polarized in the anti-Larmor sense. Such waves are nonresonant, in the same way that the uniform mode dynamic magnetization response excited by anti-Larmor circularly polarized microwave fields is nonresonant [31].

This section on the magnetostatic surface wave is concluded with a presentation of numerical results on mode profiles and mode dispersion as a function of reduced wave number kS and propagation angle ϕ. This presentation parallels the volume mode results presented in Section 4 and Fig. 6. In the surface mode frequency regime, the square bracket expressions in Eqs. (38) and (39) for $4\pi m^{0}_{y}(z)$ and

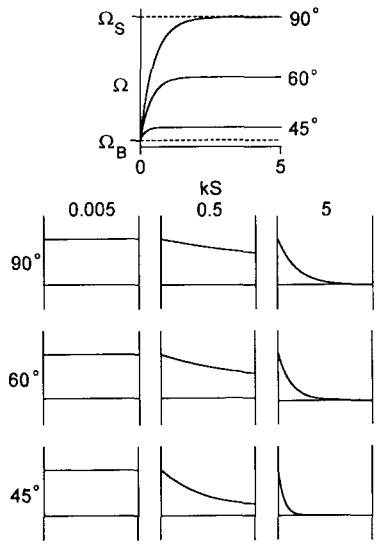

Fig. 8. Dispersion curves of reduced frequency Ω vs. reduced wavenumber kS and sets of dynamic magnetization mode profiles for $m_y^0(z)$ as a function of position z across the film for the surface mode at three values of in-plane propagation angle ϕ, as indicated. All curves are based on values for the static in-plane field H_0 and the film saturation induction $4\pi M_s$ of 1000 Oe and 1750 G, respectively, as for Fig. 4. The three columns of profiles, from left to right, are for kS values of 0.005, 0.5, and 5, respectively. From bottom to top, the dispersion curves and profiles in each set are for ϕ-values of 45°, 60°, and 90°. For consistent display, all profiles are scaled to a common value at the left $z = -S/2$ side of the film.

$4\pi m_z^0(z)$ give the z-dependent response functions for the dynamic magnetization components which correspond to the single surface mode dispersion curve branch defined through Eqs. (46) and (48). Fig. 8 shows representative sets of profiles from explicit numerical calculations for a range of propagation directions. As before, the calculations are for YIG parameters and an in-plane x-directed static magnetic field of 1000 Oe. The top diagram in Fig. 8 shows a series of surface mode dispersion curves of normalized frequency Ω vs. reduced wave number kS. These curves, from bottom to top, are for positive propagation angles of 45°, 60°, and 90°. The lower diagrams, from bottom to top, show mode profiles which correspond to these same propagation angles. The left column of profiles in Fig. 8 is for $kS = 0.005$, to approximate the condition for zero wave number k. This low $kS = 0.005$ value also corresponds to the top of the band at $\Omega \approx \Omega_B$. The center column of profiles is for $kS = 0.5$, representative of mode shapes for intermediate kS values. The right-most column of profiles in each set is for $kS = 5$, representative of mode shapes for large kS. This high kS value also corresponds to frequencies close to the top of the surface mode band at $\Omega \approx \Omega_T$ for a given propagation angle. Larger values of kS yielded profiles which were too localized at the left-side film surface to be discernable in the diagrams.

As in Fig. 6, the profile diagrams in Fig. 8 show $m_y^0(z)$ only profiles. The individual profile curves were obtained from numerical evaluations of the square bracket expression in Eq. (38) as a function of z over the range from $z = -S/2$ to $z = +S/2$. The left-most side of each profile corresponds to $z = -S/2$ and the right-most edge to $z = +S/2$. For positive propagation angles corresponding to $k_y > 0$, the surface character appears for large kS values as a localization at the left-most $z = -S/2$ surface. The profiles are all scaled to a common maximum amplitude at $z = -S/2$. As before, in order to keep the diagrams as simple as possible, $m_z^0(z)$ profiles are not shown. The m_z^0 profiles were generally smaller than the m_y^0 profiles and were of opposite sign. The smaller values reflect the ellipticity of the classical magnetization precession for in-plane magnetized films. The opposite sign corresponds to the expected Larmor sense of precession for the normal mode response. As discussed above, the polarization tends to circular in the limit of $kS \gg 1$ for propagation at $\phi = 90°$.

Fig. 8 confirms the basic properties of the surface mode obtained analytically. The surface mode dispersion curve emerges from the top of the bulk spin wave band at $\Omega = \Omega_B$ when the propagation angle exceeds the critical angle ϕ_c. Recall that for the parameters used here, the critical angle is 37.1°. The dispersion curves for all propagation angles above ϕ_c approach $\Omega = \Omega_B$ in the limit $kS \to 0$. For all angles above ϕ_c, the surface mode frequency initially increases as kS increases and then levels off at some constant value for large kS. These limiting mode frequencies for $kS \gg 1$ correspond to the Ω_U frequency parameter given in Eq. (49). In the limit of perpendicular propagation at $\phi = 90°$, Ω_U moves up to the Damon–Eshbach surface mode frequency $\Omega_S = \Omega_H + 1/2$. As evident from the trend of the dispersion curves in Fig. 8, the value of the reduced

wave number kS for saturation generally increases from a low value below $kS = 1$ for propagation angles close to ϕ_c to a value in the $kS = 2$–3 range at $\phi = 90°$. Frequency saturation for the surface mode generally occurs for much smaller values of kS than for the volume modes. From Figs. 4, 5 and 6, the volume mode frequencies approach the Ω_A limit only for large kS values on the order of 10 or more.

Turn now to the profile diagrams. The left column of profiles shows that for very low kS, one simply obtains the uniform mode response for all propagation angles above ϕ_c. Recall that precisely at the critical angle, one obtains the quasi-unpinned/quasi-pinned profile shown by the low kS, $\phi = 37.1°$ profile in the (a) part of Fig. 6 for the $n = 1$ volume mode. The effect of increasing kS on the mode profiles is readily evident from the center and right columns of profile diagrams in Fig. 8. With increasing kS, all profiles become more and more localized at the left side of the film. If either the direction of the static field or the sign of the propagation angle ϕ is reversed, the localization shifts from the left side to the right side. The localization also increases as one approaches the critical angle.

As already indicated, the mode polarizations obtained from the numerical analysis are in agreement and consistent with the analytical results presented above. All modes show Larmor rotation. In the low kS limit, the modes are elliptically polarized with an the $|m_y^0|/|m_z^0|$ ratio of Ω_B/Ω_H, the same as for ferromagnetic resonance. This is the same result as obtained for the lowest order volume mode branch below ϕ_c. In the high kS limit, the ellipticity decreases. For high kS and $\phi = 90°$, the polarization becomes circular and the mode frequency approaches $\Omega_S = \Omega_H + 1/2$.

6. The near uniform mode

The above results provide a basic review of the theory of magnetostatic modes for in-plane magnetized isotropic films and demonstrate several new or little realized features of these modes. The theory gives two quite different types of modes, volume modes and a surface mode. There is a clear critical angle effect for both types. The mode profiles show quasi-unpinned and quasi-pinned properties in various limits of propagation direction and wave number. These quasi-pinning effects appear even though there are no explicit boundary conditions on the dynamic magnetization at the film surfaces in the theory. These effects appear in both the very low kS and the very high kS limits. These effects may limit, therefore, the ranges of validity of the theory for real magnetic films with real pinning constraints at the surfaces.

Recent developments in thin film technology have led to the production of very thin magnetic films [32–34], magnetic sandwiches [35–37], and multilayer films [38] of high quality by molecular beam epitaxy. The availability of such films has resulted in, among other things, a revival of interest in the spin wave excitations in general and the magnetostatic mode excitations in particular for very thin films. The case of very thin films, on the order of a few monolayers or so in thickness, provides an extremely useful limit for a further understanding of the basic interactions which lead to the very different volume mode and surface mode behaviors discussed above. The purpose of this end section is to consider this limit.

The discussion here is limited, therefore, to the specific case $kS \ll 1$. In this limit, one may assume that for either the lowest order volume mode dispersion branch or the surface mode dispersion branch, both the dynamic microwave field and the dynamic magnetization are nearly uniform across the film cross section. This assumption, in turn, leads to significant simplifications in the analysis. One particularly useful result is a simplified equation of motion response formulation in terms of averaged dynamic fields across the film. This approach leads to a simple understanding of the role of the various dipole fields in producing volume modes below the critical angle and surface modes above the critical angle.

The specific procedure described below is due to Cochran [35,39]. One starts with a dynamic magnetization in the form of a uniform plane wave with wave vector $\boldsymbol{k}$ in the x–y film plane. One writes the components of $\boldsymbol{m}$ in the same form as before, $m_{y,z} = m_{y0,z0}(z)\exp(i[\boldsymbol{k}\cdot\boldsymbol{r} - \omega(k)t])$, but with the complex $m_{y0,z0}(z)$ amplitudes now taken as constants:

$$m_y = m_{y0}\, e^{i(k_x x + k_y y - \omega t)}, \tag{60}$$

$$m_z = m_{z0}\, e^{i(k_x x + k_y y - \omega t)}. \tag{61}$$

This form for $m_{y,z}$ amounts to a uniform mode as far as the profile across the film cross section is concerned, but with the form of a propagating wave in the x–y plane as well.

A 'near uniform mode' plane wave as defined above gives rise to a characteristic dynamic dipole field $\boldsymbol{h}$. This $\boldsymbol{h}$ field derives from the dynamic demagnetizing field associated with the uniform mode, $\boldsymbol{h}_d = -4\pi m_z \boldsymbol{e}_z$, in combination with the additional dipole field contributions due to the propagation at nonzero $\boldsymbol{k}$. This dynamic $\boldsymbol{h}$ field, when included in the torque equation of motion (1), leads to a very simple yet illuminating Ω vs. k dispersion characteristic. The frequency starts out at the uniform mode frequency $\Omega = \Omega_B$ for $k = 0$, as expected. As the wave number k is increased from zero, however, one finds that the frequency Ω associated with this 'near uniform' propagating mode (1) decreases with k if the propagation angles is below the DE critical angle ϕ_c and (2) increases with k for propagation angles above ϕ_c. In contrast with the discontinuous nature of the volume mode-to-surface mode changeover evident from the conventional DE analysis presented in previous sections, this near uniform mode analysis demonstrates the continuous nature of the changeover as a direct result of changes in the dipole fields for the propagating modes. This point will be evident from the results shown below.

In the present problem, one starts with the near uniform mode $\boldsymbol{m}$ response given in Eqs. (60) and (61), and proceeds to solve Maxwell's equations in the magnetostatic approximation for the resulting dipole field $\boldsymbol{h}$. Here, as in the DE theory, a straightforward if somewhat tedious solution is possible by means of a separation of variables scalar potential approach. The details of the analysis are given in Appendix B. Only the key equations and results are given below.

One assumes scalar potential functions inside and outside the film according to

$$\psi^i(x,y,z) = f^i(z)\, e^{i(k_x x + k_y y)} \quad (|z| < S/2) \tag{62}$$

and

$$\psi^e(x,y,z) = f^e(z)\, e^{i(k_x x + k_y y)} \quad (|z| > S/2). \tag{63}$$

The f-functions serve the same role here that the Z-functions serve in the DE theory. The dynamic field is given by $\boldsymbol{h}(\boldsymbol{r},t) = \nabla\psi(\boldsymbol{r})\exp[-i\omega t]$. One then solves the $\nabla \cdot \boldsymbol{b} = 0$ Maxwell equation outside the film, given as $\nabla^2\psi^e = 0$, and inside the film, given as $\nabla^2\psi^i \exp[-i\omega t] = -4\pi\nabla \cdot \boldsymbol{m}$, subject to the usual boundary conditions on $\boldsymbol{b}$ and $\boldsymbol{h}$ at the film surfaces. One obtains, after somewhat tedious algebra, expressions for the scalar potential f-functions. The $f^i(z)$ function obtained from this procedure is

$$f^i(z) = \frac{4\pi i m_{y0} \sin\phi}{k} - \frac{4\pi\, e^{-kS/2}}{k} \times \left[i m_{y0} \sin\phi \cosh(kz) + m_{z0} \sinh(kz) \right]. \tag{64}$$

With the dynamic $\boldsymbol{h}$ defined as before, according to $h_{y,z} = h_{y0,z0}(z)\exp(i[\boldsymbol{k}\cdot\boldsymbol{r} - \omega(k)t])$, one then obtains the full z-dependent $\boldsymbol{h}(\boldsymbol{r},t)$ from Eq. (64) with $h_{y0}(z) = ik_y f^i(z)$ and $h_{z0}(z) = df^i(z)/dz$.

It is important to emphasize that the uniform profile assumption for $\boldsymbol{m}$ embodied in Eqs. (60) and (61) is valid only in the $kS \ll 1$ limit. This means that any z-dependences for $h_{y0,z0}(z)$ should be small. The final step in the field analysis is to obtain the spatially averaged $h_{y0}(z)$ and $h_{z0}(z)$ field amplitudes across the film. The final result is two rather simple expressions for the z-averaged $\langle h_{y0}\rangle$ and $\langle h_{z0}\rangle$ field amplitudes which are associated with the propagating $\boldsymbol{m}$ wave defined through Eqs. (60) and (61). With k_x and k_y expressed as $k_x = k\cos\phi$ and $k_y = k\sin\phi$, these fields are obtained as

$$\langle h_{y0}\rangle = -2\pi m_{y0}(kS)\sin^2\phi \tag{65}$$

and

$$\langle h_{z0}\rangle = -4\pi m_{z0} + 2\pi m_{z0}(kS). \tag{66}$$

In terms of these spatially averaged field amplitudes, the 'near uniform mode' propagating dipole field which corresponds to the near uniform mode propagating magnetization wave in Eqs. (60) and (61) is now given by $h_{y,z} = \langle h_{y0,z0}\rangle \exp(i[\boldsymbol{k}\cdot\boldsymbol{r} - \omega(k)t])$. It is important to note that the connections between $\boldsymbol{m}$ and $\boldsymbol{h}$ contained in Eqs. (65) and (66) derive solely from the assumed form for $\boldsymbol{m}$ and Maxwell's equations. No magnetic torque equation or magnetic response, as in Eqs. (1) or (2), is involved. Eqs. (65) and (66) are the same as given by Cochran [39] and reduce to Eqs. (A6a) and (A6b) in Appendix A of Cochran et al. [35] for the case of $\phi = 90°$.

Eqs. (65) and (66) have a simple physical interpretation. Consider $\langle h_{y0} \rangle$ first. This is the dynamic field component in the plane of the film and perpendicular to the static field $\boldsymbol{H}_0$ and static magnetization $\boldsymbol{M}_s$. In the limit of zero wave number, or $kS = 0$, $\langle h_{y0} \rangle$ vanishes as one would expect, due to the zero in-plane demagnetizing factor for the infinite film. As kS increases, however, this field can become nonzero as long as the direction of propagation is not along $\boldsymbol{H}_0$ and $\boldsymbol{M}_s$. Under such conditions, h_y is 180° out of phase with m_y and scales with $k\sin^2\phi$. In the bulk $kS \gg 1$ limit, the m_y wave of Eq. (60) would lead to an h_y field of $-4\pi m_{y0}\sin^2\phi$, which corresponds to the $4\pi M_s \sin^2\theta_k$ effective field term in the spin wave dispersion relation of Eq. (30). In both cases, $\langle h_y \rangle$ has the same basic origin in a nonvanishing $\nabla \cdot \boldsymbol{m}$ inside the material when ϕ or θ_k is nonzero.

Turn now to $\langle h_{z0} \rangle$. The $-4\pi m_{z0}$ term in Eq. (66) represents the usual thin film shape demagnetizing field associated with m_{z0} in the $kS \to 0$ uniform mode limit. The key new result in Eq. (66) is that the increase in the wave number k for propagation in any direction serves to reduce this dynamic demagnetizing field component. Eq. (66) is valid, of course, only in the limit $kS \ll 1$. In the opposite limit, $kS \gg 1$, the wavelength is sufficiently short so that the shape demagnetizing fields due to the rapidly oscillating $\nabla \cdot \boldsymbol{m}$ at the film surfaces average to zero. This is the basis of the spin wave limit for which sample shape effects may be neglected entirely.

The final step in the near uniform mode analysis is to incorporate the dynamic fields specified by Eqs. (66) and (67) and the dynamic magnetization of Eqs. (60) and (61) into the torque equation of motion, Eq. (1), along with the static field $\boldsymbol{H}_0$ and the static magnetization $\boldsymbol{M}_s$. Note that in the DE theory, the equation of motion was used to connect $\boldsymbol{m}$ and $\boldsymbol{h}$ in the very first stages of the analysis, and Maxwell's equations were then used to obtain the normal mode dispersion properties. The Cochran approach takes the opposite tack. Here, Maxwell's equations are used to connect $\boldsymbol{m}$ and $\boldsymbol{h}$ to obtain the relations shown in Eqs. (66) and (67), and the torque equation is then used to obtain the normal mode dispersion. This later approach, of course, works only because $\boldsymbol{m}$ is taken to be near uniform and kS is small. The resulting dispersion, therefore, gives the normal mode frequency for the near uniform mode in the limit of small kS and frequencies close to Ω_B.

Eq. (1), with $\boldsymbol{M} = M_s \boldsymbol{e}_x + m_y \boldsymbol{e}_y + m_z \boldsymbol{e}_z$ and $\boldsymbol{H} = H_0 \boldsymbol{e}_x + \langle h_y \rangle \boldsymbol{e}_y + \langle h_z \rangle \boldsymbol{e}_z$ according to Fig. 1 and Eqs. (60), (61), (66), and (67), yields a near uniform mode frequency $\omega(k)$ given by

$$\omega(k) = \gamma \sqrt{H_{ey} H_{ez}}, \tag{67}$$

where H_{ey} and H_{ez} represent effective stiffness fields of the form

$$H_{ey} = H_0 + 2\pi M_s(kS)\sin^2\phi \tag{68}$$

and

$$H_{ez} = H_0 + 4\pi M_s - 2\pi M_s(kS). \tag{69}$$

In the $kS \to 0$ limit, Eq. (67) reduces to the usual ferromagnetic resonance frequency $\omega_B = [H_0(H_0 + 4\pi M_s)]^{1/2}$, or in terms of reduced frequency, Ω_B. This is the same result as in the DE theory. For nonzero kS, however, one obtains a normal mode frequency which may initially increase or decrease from ω_B, depending on the propagation angle ϕ. To first order in kS, and in terms of the reduced frequency parameter Ω, one obtains

$$\Omega = \Omega_B + \frac{kS}{4\Omega_H \Omega_B}\left[\Omega_B^2 \sin^2\phi - \Omega_H^2\right]. \tag{70}$$

This near uniform mode dispersion result demonstrates the effect of the dynamic dipole fields through their respective contributions to the H_{ey} and H_{ez} stiffness fields in producing an increasing or decreasing frequency as a function of k. If the square bracket term in Eq. (70), which controls the sign of this k-dependence, is set to zero, one obtains the same critical angle obtained previously for both the DE volume modes and the surface mode. The present results make it clear that the volume to surface branch conversion for the near uniform mode is specifically due to the different signs and ϕ-dependences for the $\langle h_y \rangle$ and $\langle h_z \rangle$ dynamic demagnetizing fields. This conversion is not a discontinuous process, as one might conclude from the separate volume and surface mode aspects of the DE analysis. It represents, rather, a continuous process as the stiffness field due to the $\langle h_y \rangle$ field becomes more and more negative as ϕ increases, and the corresponding contribution to the H_{ey} stiffness field be-

comes more and more positive. The critical angle ϕ_c simply marks the point at which the positive $\langle h_y \rangle$ stiffness field contribution exactly balances the negative $\langle h_z \rangle$ contribution. The slope of the Ω vs. kS function in Eq. (70) is the same, of course, as obtained from the DE theory in the $kS \ll 1$ limit.

Acknowledgements

This work was started while one of the authors (CEP) was on sabbatical in 1984/1985 and supported in part by the Department of Physics, Simon Fraser University, Burnaby, BC, Canada. The authors gratefully acknowledge Dr. J.F. Cochran of Simon Fraser University for helpful discussions during the course of this work and, in particular, for pointing out the simple form of the dipole fields which result in the near uniform mode theory. Drs. P. Kabos, M. Chen, M. Mendik, I. Laulicht and M.A. Tsankov are acknowledged for helpful comments on the manuscript. The work was supported in part by the National Science Foundation under Grant Nos. DMR-8921761 and DMR-9400276, the U.S. Army Research Office under Grant No. DAAL03-91-G-0327, and the Office of Naval Research, Grant Nos. N00014-90-J-4078 and N00014-94-1-0096.

Appendix A. Magnetostatic approximation

The magnetostatic approximation is one of the basic approximations in the standard theories for spin wave and magnetostatic wave excitations in magnetic materials. The analytic form of the approximation is contained in the $\nabla \times \boldsymbol{h} = 0$ equation introduced in Section 2. The approximation is termed 'magnetostatic' because the $\nabla \times \boldsymbol{h} = 0$ condition is valid only in the limit of low frequency, relative to the frequency of light, for a given wave number k. For a magnetic excitation of frequency ω_k, this condition amounts to $\omega_k \ll ck$. Conversely, for a given frequency ω_k, the wave number k for the mode will be much greater than the light wave number k_0 at the same frequency. The purpose of this appendix is to make clear the connections between the magnetostatic condition and the $\nabla \times \boldsymbol{h} = 0$ equation.

Consider the full set of Maxwell equations for the dynamic electric and magnetic fields, $\boldsymbol{e}(\boldsymbol{r},t)$ and $\boldsymbol{h}(\boldsymbol{r},t)$, and the dynamic magnetization $\boldsymbol{m}(\boldsymbol{r},t)$ for a magnetic insulator with a scalar dielectric constant ϵ:

$$\nabla \cdot \boldsymbol{e}(\boldsymbol{r},t) = 0, \tag{A1}$$

$$\nabla \times \boldsymbol{e}(\boldsymbol{r},t) = -\frac{1}{c}\frac{\partial}{\partial t}\left[\boldsymbol{h}(\boldsymbol{r},t) + 4\pi \boldsymbol{m}(\boldsymbol{r},t)\right], \tag{A2}$$

$$\nabla \cdot \left[\boldsymbol{h}(\boldsymbol{r},t) + 4\pi \boldsymbol{m}(\boldsymbol{r},t)\right] = 0, \tag{A3}$$

$$\nabla \times \boldsymbol{h}(\boldsymbol{r},t) = \frac{\epsilon}{c}\frac{\partial}{\partial t}\boldsymbol{e}(\boldsymbol{r},t). \tag{A4}$$

Here, c denotes the speed of light in free space.

The usual approach in the magnetostatic approximation is first to neglect the time derivative driving term and write Eq. (A4) as

$$\nabla \times \boldsymbol{h}(\boldsymbol{r},t) = 0. \tag{A5}$$

One then considers plane wave solutions for $\boldsymbol{h}(\boldsymbol{r},t)$ and $\boldsymbol{m}(\boldsymbol{r},t)$ with frequency ω_k and wave vector $\boldsymbol{k}$:

$$\boldsymbol{h}(\boldsymbol{r},t) = \boldsymbol{h}_k e^{i(\boldsymbol{k}\cdot\boldsymbol{r} - \omega_k t)}, \tag{A6a}$$

$$\boldsymbol{m}(\boldsymbol{r},t) = \boldsymbol{m}_k e^{i(\boldsymbol{k}\cdot\boldsymbol{r} - \omega_k t)}. \tag{A6b}$$

Eqs. (A5) and (A6), together with Eq. (A3), lead immediately to the well-known expression for the dipole field $\boldsymbol{h}_k$ associated with a propagating spin wave of wave vector $\boldsymbol{k}$ and with a dynamic magnetization amplitude $\boldsymbol{m}_k$:

$$\boldsymbol{h}_k \approx -\frac{4\pi}{k^2}\boldsymbol{k}(\boldsymbol{k}\cdot\boldsymbol{m}_k). \tag{A7}$$

The procedure here will be to start with the full set of Maxwell equations as listed above, develop a general expression for $\boldsymbol{h}_k$, and demonstrate that this expression reduces to Eq. (A7) in the limit $k \gg k_0$.

From Eqs. (A1)–(A4), the wave equation for $\boldsymbol{h}(\boldsymbol{r},t)$ is obtained as

$$\nabla^2 \boldsymbol{h}(\boldsymbol{r},t) - \frac{\epsilon}{c^2}\frac{\partial^2}{\partial t^2}\boldsymbol{h}(\boldsymbol{r},t) = -4\pi\nabla\left[\nabla \cdot \boldsymbol{m}(\boldsymbol{r},t)\right] + 4\pi\frac{\epsilon}{c^2}\frac{\partial^2}{\partial t^2}\boldsymbol{m}(\boldsymbol{r},t). \tag{A8}$$

Consider once more the plane wave solutions for $\boldsymbol{h}(\boldsymbol{r},t)$ and $\boldsymbol{m}(\boldsymbol{r},t)$ in Eq. (A6). From Eq. (A8), the relation between the time-independent amplitudes $\boldsymbol{h}_k$ and $\boldsymbol{m}_k$ is given by

$$\boldsymbol{h}_k = -\frac{1}{k^2 - k_0^2} 4\pi \boldsymbol{k}(\boldsymbol{k} \cdot \boldsymbol{m}_k) + \frac{k_0^2}{k^2 - k_0^2} 4\pi \boldsymbol{m}_k. \tag{A9}$$

As already indicated, k_0 denotes the wave number for ordinary electromagnetic waves propagating with the same frequency ω_k in the medium:

$$k_0 = \frac{\omega_k}{c}\sqrt{\epsilon}. \tag{A10}$$

For typical ferrites with a dielectric constant $\epsilon = 10$ and a spin wave frequency $\omega_k = 10$ GHz, one obtains a numerical value for k_0 of 6.6 rad/cm.

The two terms on the right hand side of Eq. (A9) have different physical origins. The $\boldsymbol{k}(\boldsymbol{k} \cdot \boldsymbol{m}_k)$ term derives from the microscopic magnetic dipole–dipole interaction. The $4\pi \boldsymbol{m}_k$ term derives from the time derivative of the electric field and, therefore, may be called the electromagnetic propagation term. In a situation where the condition $|k| \gg k_0$ is satisfied, the contribution from the $4\pi \boldsymbol{m}_k$ term in Eq. (A9) is negligible. In this limit, only the dipole field contribution remains and right hand side of Eq. (A9) can be approximated by the first term only. In this limit, the $\boldsymbol{h}_k$ expression of Eq. (A7) is obtained. This is the form of the dipole field which is utilized extensively in classical spin wave theory.

It is important to note that there is *no upper limit* on the range of k for this approximation. There is an upper limit on k, on the order of 10^5–10^6 rad/cm, for the neglect of exchange. Some workers incorrectly make this restriction part of the magnetostatic approximation. The only limitation for the validity of Eq. (A7) is the condition $|k| \gg k_0$.

As pointed out above, use of the $\nabla \times \boldsymbol{h} = 0$ condition also leads to the operational spin wave dipole field expression of Eq. (A7). Hence, this $\nabla \times \boldsymbol{h} = 0$ condition is often called the magnetostatic approximation. As evident from the above analysis, however, the 'magnetostatic' nature of the approximation, e.g. $|k| \gg k_0$ for a given frequency ω_k or $\omega_l = ck/\sqrt{\varepsilon} \gg \omega_k$ for a given wave number k, is apparent only if the full Maxwell equations are used as a starting point for the analysis.

Appendix B. Near uniform mode analysis

The 'near uniform' mode treatment outlined in Section 6 provides insight into the origins of the backward volume wave and surface wave character of the Damon–Eshbach modes in terms of the dipole fields for propagating 'plane waves' in the film. The term 'near uniform' means that the dynamic magnetization is assumed to be a 'plane wave' within the confines of the film, that is, a propagating wave which has a wave front of constant amplitude across the film.

Consider a thin ferromagnetic film which is magnetized in plane by the application of an external magnetic field as in Fig. 1, with the static magnetization $\boldsymbol{M}_s$ and the static field $\boldsymbol{H}_0$ in the x-direction as before. As indicated in Section 6, the starting point of the analysis is with y- and z-components of the propagating dynamic magnetization of the form

$$m_y = m_{y0}\, e^{i(k_x x + k_y y - \omega t)} \tag{B1}$$

and

$$m_z = m_{z0}\, e^{i(k_x x + k_y y - \omega t)}, \tag{B2}$$

where m_{y0} and m_{z0} are constants. The wave vector components k_x and k_y defined through Fig. 1 and Eq. (9) are the same as in Section 2. Eqs. (B1) and (B2) represent the 'near uniform' propagating mode. The $\boldsymbol{m}$ response is 'uniform' across the film cross section, that is, there is no z-dependence for m_{y0} or m_{z0}.

The $\nabla \times \boldsymbol{h} = 0$ condition under the magnetostatic approximation allows the introduction of a scalar potential ψ in the same way as in the DE theory, according to $\boldsymbol{h}(\boldsymbol{r},t) = \nabla\psi(\boldsymbol{r})\exp[-i\omega t]$. The key difference from the DE theory comes in the treatment of the $\nabla \cdot \boldsymbol{b} = 0$ condition. In the DE formalism, one uses the relation $\nabla \cdot \boldsymbol{b} = \nabla \cdot (\boldsymbol{h} + 4\pi \boldsymbol{m}) = 0$, the magnetic susceptibility connection between $\boldsymbol{m}$ and $\boldsymbol{h}$ from Eq. (2), and the scalar potential form for $\boldsymbol{h}$ to obtain the basic formal DE equations given in Section 2. In this near uniform mode case, $\boldsymbol{m}(\boldsymbol{r},t)$ is specified explicitly according to Eqs. (B2) and (B3). The $\nabla \cdot (\boldsymbol{h} + 4\pi \boldsymbol{m}) = 0$ condition, along with Eqs. (B2) and (B3), give simple differential equations for $\psi(\boldsymbol{r})$ directly. Define, as in the DE theory, different scalar potentials inside the film and outside the film

as $\psi^{i}(\boldsymbol{r})$ and $\psi^{e}(\boldsymbol{r})$, respectively. Inside the film, one obtains

$$\nabla^2\psi^{i}(\boldsymbol{r}) = -4\pi i k_y m_{y0}\, e^{i(k_x x + k_y y)}. \tag{B3}$$

Outside the film, one obtains

$$\nabla^2\psi^{e}(\boldsymbol{r}) = 0. \tag{B4}$$

In order to solve Eqs. (B3) and (B4), one proceeds with a standard separation of variables approach according to

$$\psi^{i,e}(x,y,z) = f^{i,e}(z)\, e^{i(k_x x + k_y y)}, \tag{B5}$$

where the $f^{i}(z)$ and $f^{e}(z)$ functions apply for $|z| < S/2$ and $|z| > S/2$, respectively. Note that the $f^{i}(z)$ and $f^{e}(z)$ functions play the same role in the near uniform mode analysis that the $Z^{i}(z)$ and $Z^{e}(z)$ play in the DE theory.

Substitution of the above trial functions into Eqs. (B3) and (B4) leads to ordinary differential equations for $f^{i}(z)$ and $f^{e}(z)$:

$$\frac{d^2 f^{i}(z)}{dz^2} - k^2 f^{i}(z) = -4\pi i k_y m_{y0}, \tag{B6}$$

$$\frac{d^2 f^{e}(z)}{dz^2} - k^2 f^{e}(z) = 0. \tag{B7}$$

The propagation wave number $k = (k_x^2 + k_y^2)^{1/2}$ is the same as in Section 2. The general solution to Eq. (B6) is

$$f^{i}(z) = a e^{+kz} + b e^{-kz} + \frac{4\pi i m_{y0} k_y}{k^2} \quad (|z| < S/2). \tag{B8}$$

With the requirement that all dynamic fields decay to zero at large distances from the film, one obtains solutions to Eq. (B7) as

$$f^{e}(z) = c e^{-kz} \quad (z > +S/2) \tag{B9}$$

and

$$f^{e}(z) = d e^{+kz} \quad (z < -S/2). \tag{B10}$$

It is important to remember that the above analysis is valid only in the limit $kS \ll 1$. In this limit, the $f^{i}(z)$ profile given in Eq. (B8) is nearly uniform, as is the $Z^{i}(z)$ profiles of Eq. (12) or Eq. (43) in the DE theory for this same limit. The $f^{e}(z)$ profiles in Eqs. (B9) and (B10) are similar in form to the $Z^{e}(z)$ profiles of Eqs. (13) and (14).

As in the DE analysis, the next step is to impose the usual electromagnetic boundary conditions on $\boldsymbol{h}$ and $\boldsymbol{b}$ at the film surfaces at $z = \pm S/2$. The $\boldsymbol{h}$ fields are obtained from the $\psi^{i}(\boldsymbol{r})$ and $\psi^{e}(\boldsymbol{r})$ functions defined above and the scalar potential connection $\boldsymbol{h}(\boldsymbol{r},t) = \nabla\psi(\boldsymbol{r})\exp[-i\omega t]$. The dynamic magnetic induction $\boldsymbol{b}$ is then specified by $\boldsymbol{b} = \boldsymbol{h} + 4\pi\boldsymbol{m}$. The requirements that the components of $\boldsymbol{h}$ parallel to the film surfaces, h_x and h_y, and the component of $\boldsymbol{b}$ perpendicular to the film surface, b_z, be continuous at $z = \pm S/2$ leads to four equations in the four unknown scalar potential parameters, a, b, c, and d. These equations may be written concisely in matrix form as

$$\begin{bmatrix} e^{kS} & 1 & -1 & 0 \\ 1 & e^{kS} & 0 & -1 \\ e^{kS} & -1 & 1 & 0 \\ 1 & -e^{kS} & 0 & -1 \end{bmatrix} \begin{bmatrix} a \\ b \\ c \\ d \end{bmatrix} = \frac{-4\pi\, e^{kS/2}}{k} \begin{bmatrix} \frac{i k_y m_{y0}}{k} \\ \frac{i k_y m_{y0}}{k} \\ m_{z0} \\ m_{z0} \end{bmatrix}. \tag{B11}$$

Eq. (B11) can be solved for a, b, c, and d. One may then construct the internal and external scalar potential functions explicitly. For the purposes of this analysis, only the $f^{i}(z)$ function and the corresponding internal scalar potential function $\psi^{i}(\boldsymbol{r})$ are needed. The a parameter in $f^{i}(z)$ is obtained by simply adding the row 1 and row 3 equations contained in Eq. (B11). Similarly, the b parameter is obtained by subtracting the row 4 equation from the row 2 equation. With $k_y = k\sin\phi$, one obtains the $f^{i}(z)$ function given in Eq. (64) of Section 6.

The dynamic magnetic field $\boldsymbol{h}$ inside the film is then obtained from the full scalar potential and the $\boldsymbol{h}(\boldsymbol{r},t) = \nabla\psi^{i}(\boldsymbol{r})\exp[-i\omega t]$ prescription. Recall the form of $\boldsymbol{h}(\boldsymbol{r},t)$ in component form, defined by $h_{y,z} = h_{y0,z0}(z)\exp(i[\boldsymbol{k}\cdot\boldsymbol{r} - \omega(k)t])$. As indicated in Section 6, the z-dependent $h_{y0,z0}(z)$ amplitudes are specified in terms of the the $f^{i}(z)$ function by $h_{y0}(z) = i k_y f^{i}(z)$ and $h_{z0}(z) = d f^{i}(z)/dz$. Just as $f^{i}(z)$ is a fairly complicated function, the full $h_{y0,z0}(z)$ functions are also complicated. However,

in the range of kS for which the present analysis is valid, $kS \ll 1$, these functions may be greatly simplified. This is accomplished by expanding the $\exp[-kS/2]$, $\cosh(kz)$, and $\sinh(kz)$ functions which appear in $h_{y0,z0}(z)$ in Taylor series and retaining only terms in kz or $kS/2$ to first order. This first order expansion in kz and $kS/2$ yields the $h_{y0,z0}(z)$ expressions given below:

$$h_{y0}(z) = -2\pi m_{y0}(kS)\sin^2\phi - 4\pi i m_{z0}(1-kS/2)(kz)\sin\phi, \quad \text{(B12)}$$

$$h_{z0}(z) = -4\pi m_{z0} + 2\pi m_{z0}(kS) - 4\pi i m_{y0}(1-kS/2)(kz)\sin\phi. \quad \text{(B13)}$$

The final step in the near uniform mode dipole field analysis is to note that the last terms in Eqs. (B12) and (B13) are both small. This means that the $h_{y0,z0}(z)$ are nearly uniform across the film cross section. Further, these terms are odd functions in z. This means that if one considers the spatial averages of $h_{y0,z0}(z)$ across the film, the only surviving terms will be the leading terms in Eq. (B12) and the leading two terms in Eq. (B13), respectively. One obtains, therefore, spatially averaged propagating dipole field amplitudes $\langle h_{y0}\rangle$ and $\langle h_{z0}\rangle$ which correspond to these terms only. These amplitudes are as specified in Eqs. (65) and (66) of Section 6.

References

[1] T. Holstein and H. Primakoff, Phys. Rev. 58 (1940) 1098.
[2] J.H.E. Griffiths, Nature 158 (1946) 670.
[3] C. Kittel, Phys. Rev. 73 (1948) 155.
[4] L.R. Walker, Phys. Rev. 105 (1957) 390.
[5] P. Röschmann and H. Dötsch, Phys. Stat. Sol. (b) 82 (1977) 11.
[6] R.W. Damon and J.R. Eshbach, J. Phys. Chem. Solids 19 (1961) 308.
[7] J.C. Sethares, RADC-TR-83-15, in: Proceedings of the 1981 RADC Microwave Magnetics Technology Workshop, June 10–11, 1981, Rome Air Development Center, Air Force Systems Command (Griffiss Air Force Base, New York, 1983).
[8] J.P. Parekh, Circ. Syst. Signal Proc. 4 (1&2) (1985).
[9] D.D. Stancil, Theory of Magnetostatic Waves (Springer Verlag, New York, 1993).
[10] G.P. Rodrique, IEEE Trans. Microwave Theory Tech. 11 (1963) 351.
[11] C. Vittoria, J. Magn. Magn. Mater. 21 (1980) 109.
[12] C.E. Patton, IEEE Trans. Magn. 24 (1988) 2024.
[13] J. Magn. Magn. Mater. 126 (1994).
[14] B. Schneider, Phys. Stat. Sol. (b) 51 (1972) 325.
[15] B. Schneider, Phys. Stat. Sol. (b) 66 (1974) 99.
[16] H. Reimann and F. Waldner, IEEE Trans. Magn. 15 (1979) 1720.
[17] G. Rupp, W. Wettling, R.S. Smith and W. Jantz, J. Magn. Magn. Mater. 45 (1984) 404.
[18] S.P. Li and L.E. Cross, Phys. Stat. Sol. (b) 159 (1990) 861.
[19] S.N. Baipai, R.W. Weinert and J.D. Adam, J. Appl. Phys. 58 (1985) 990.
[20] A.N. Slavin and Y.K. Fetisov, Zh. Tekh. Fiz. 58 (1988) 2210 [Sov. Phys. Tech. Phys. 33 (1988) 1343].
[21] M. Sparks, Phys. Rev. B 1 (1970) 3831.
[22] R.E. DeWames and T. Wolfram, J. Appl. Phys. 41 (1970) 987.
[23] T. Wolfram and R.E. DeWames, Phys. Rev. B 4 (1971) 3125.
[24] B.A. Kalinikos, IEE Proc. (London) 127 (H1) (1980) 4.
[25] B.A. Kalinikos and A.N. Slavin, J. Phys. C 19 (1986) 7013.
[26] C. Kittel, Phys. Rev. 110 (1958) 1295.
[27] G.T. Rado and J.R. Weertman, J. Phys. Chem. Solids 11 (1959) 315.
[28] C.E. Patton, Phys. Rep. 103 (1984) 251.
[29] B. Lax and K.J. Button, Microwave Ferrites and Ferrimagnetics (McGraw-Hill, New York, 1962) p. 150.
[30] M. Sparks, Ferromagnetic Relaxation Theory (McGraw-Hill, New York, 1964).
[31] C.E. Patton, in: Magnetic Oxides, ed. D.J. Craik (John Wiley, London, 1975) ch. 10.
[32] G.A. Prinz and J.J. Krebs, Appl. Phys. Lett. 39 (1981) 397.
[33] G.A. Prinz, G.T. Rado and J.J. Krebs, J. Appl. Phys. 53 (1982) 2087.
[34] C. Liu and S.D. Bader, J. Magn. Magn. Mater. 93 (1991) 307.
[35] J.F. Cochran, J. Rudd, W.B. Muir, B. Heinrich and Z. Celinski, Phys. Rev. B 42 (1990) 508.
[36] J.J. Krebs, P. Lubitz, A. Chaiken and G.A. Prinz, Phys. Rev. Lett. 63 (1989) 1645.
[37] J.J. Krebs, P. Lubitz, A. Chaiken and G.A. Prinz, J. Appl. Phys. 67 (1990) 5920.
[38] B. Heinrich, Z. Celinski, J.F. Cochran, A.S. Arrott and K. Myrtle, J. Appl. Phys. 70 (1991) 5769.
[39] J.F. Cochran, Section 3.2 in: Ultrathin Magnetic Structures II, eds. J.A.C. Bland and B. Heinrich (Springer Verlag, Heidelberg, 1994) pp. 222–257.